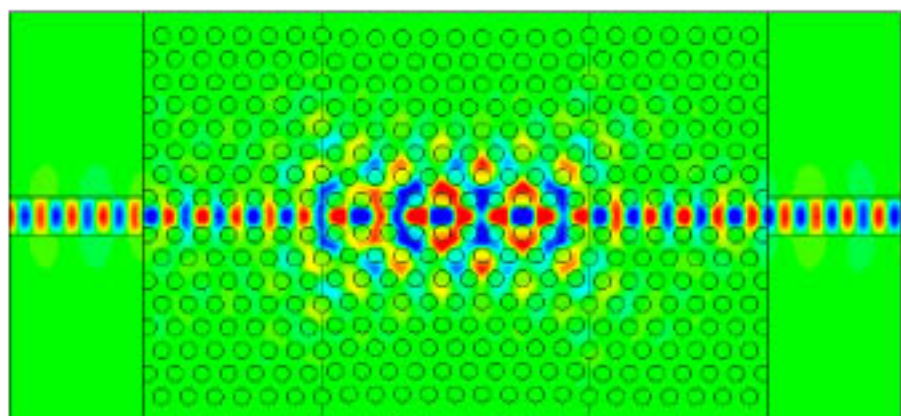Alexander Petrov

Slow light photonic crystal line-defect waveguides

Slow light
photonic crystal
line-defect waveguides

Vom Promotionsausschuss der

Technischen Universität Hamburg-Harburg

zur Erlangung des akademischen Grades

Doktor der Naturwissenschaften

genehmigte Dissertation

von

Alexander Petrov

aus

Sankt Petersburg

2008

Gutachter:

Prof. Dr. Manfred Eich (TU Hamburg-Harburg)

Pror. Dr. Ernst Brinkmeyer (TU Hamburg-Harburg)

Tag der mündlichen Prüfung:

16. November 2007

Contents

1. Introduction

Optical fibers and waveguides are gradually substituting the metal wire connections [1]. They provide larger bandwidth at high interference immunity and lack of emission. As the data transmission rate is increasing the optical connection moves from long range to enterprise network [2] and it is even on the way to enter the domain of chip-to-chip and on-chip communication [3]. This trends strengthen the demand for miniaturization and integration of optical signal transmission components, which include waveguides, modulators, photodetectors, switches and Wavelength-Division-Multiplexing (WDM) elements. Many of these components are based on the phase properties of optical signals. Tunable phase shift is the basis for Mach-Zehnder interferometers, which constitute optical switches and modulators [4]. Tunable time delay is necessary for the optical buffering in routers and synchronization components [5], where an optical signal should be stored and released after a certain period of time. And the dispersion accumulated in the optical fiber should be compensated in dispersive elements with opposite sign of dispersion [1].

As will be shown in this thesis the small group velocity of light in certain structures can be used to dramatically decrease the size of phase shift, time delay, and dispersion compensation components. These structures, also called as slow light structures, have received a lot of attention in recent years [6][7][8][9][10][11]. Going in parallel with the development of Electromagnetically Induced Transperency (EIT) [12][13][14], the slow light structures demonstrate larger bandwidth [15] and proven microscale implementation [7][16][17]. The functional length of the optical components can be decreased proportional to the group velocity reduction. Thus, where conventional units require several centimeters long structures, the tenfold group velocity reduction decreases their lengths to millimeter length.

1.1   Photonic crystal line defect waveguides in SOI

Different slow light structures were presented recently including Bragg stack at the band edge [10], coupled cavity waveguides [18] and photonic crystal line-defect waveguides [6][7]. Every of the named structures has its advantages and disadvantages.

We discuss in this thesis the photonic crystal line-defect waveguides which demonstrate some superior properties. Photonic Crystals (PCs) are periodically structured dielectric materials with period in the range of the photon wavelength [19][20][21][22]. Line-defects in photonic crystals can guide light due to the photonic band gap effect [6][23][24], different to the conventional total internal reflection. The recent advantages in manufacturing techniques lead to substantial loss reduction in such waveguides to approximately 1dB/mm [16][25][26]. Since the slow light effect was first time demonstrated in line-defect waveguides by Notomi *et al.* [6] many publications appeared concerning different possible applications. They correspond to the areas named above: increased phase shift [17][27], large tunable time delays [7][8][15][28], large dispersion [29].

On the other hand, PC line-defect waveguides can be implemented in the Silicon-on-Insulator (SOI) system, which has many advantages. First of all, the index contrast of silicon to air is sufficient for a pronounced Photonic Band Gap (PBG) effect. In this PBG frequency range there is sufficient place for the line-defect modes with engineered dispersion relation. And the same index contrast in the vertical direction opens enough space below the light cone [30]. Secondly, the SOI system is compatible with conventional silicon chip manufacturing technology and allows simple integration of optical and electronic components on the same chip [31][32]. There are already successful examples of optical modulators [17][33], Raman lasers [34] and Wavelength Division Multiplexing (WDM) components [35] integrated in SOI. Slow light in SOI structure would be an important accomplishment of this technology [7].

1.2 Goals and outline of this thesis

1.2.1 Goals

The goal of this work is to investigate different aspects of small group velocity in PC line-defect waveguides. Based on various simulation approaches and theoretical approximations four major issues of slow light are considered:
- small group velocity with vanishing dispersion
- large second order dispersion
- coupling to small group velocity modes
- disorder induced losses

More specifically, the first goal was to understand the mechanism responsible for small group velocity in line-defect waveguides and the ways to control it. This understanding opens possibilities for the tunable phase shift and time delay. At the same time it is important to keep the second order dispersion low at small group velocity bandwidth. Otherwise the impulse distortion will deteriorate the small group velocity device performance. The aim for time delay was approximately 1 ns in a 1 mm long structure on a 100 GHz bandwidth. This requires the propagation velocity equal to 0.003 speed of light in vacuum.

The second goal was to investigate the possibilities for dispersion compensation in line-defect waveguides of millimeter length. The typical length between reproducers in the optical long distance network is 100 km. The dispersion accumulated in a 100 km fiber equals approximately to 2000 ps/nm. To compensate the effect of the fiber dispersion a compensator is required with -2000 ps/nm/mm dispersion. The same as for time delay device the higher order dispersion should be avoided. Two approaches are discussed in this thesis. The dispersion is caused by the different time delay of the adjacent wavelengths. This time delay difference can be achieved by different propagation velocity or different propagation length, which require modified dispersion relation or chirped structure correspondingly.

The third goal was to find an efficient coupling approach from strip dielectric waveguide into a slow light line-defect waveguide. The direct butt-coupling of such waveguides leads to extensive losses and reflections. Thus, a special mode converter should be designed, where the strip waveguide mode would be adjusted to the slow light mode.

The last goal of this thesis was aimed at the imperfection tolerance of the slow light structures. Inaccuracies, defects and boundary roughness in the PC structures due to imperfect manufacturing can lead to scattering losses of the propagating optical mode. The effect of this scattering on the transmission and time delay properties of the slow light waveguides was investigated.

All the above named goals should be fulfilled on the bandwidth of a single WDM channel of approximately 100 GHz (0.75 nm).

1.2.2 Outline

The slow light issues discussed in the previous paragraph will be presented in the following chapters:

In chapter 2, the background information about PC line-defect waveguides and their simulations is discussed. Line-defect waveguide parameters and dispersion relations are presented. Three simulation approaches are described: Transfer Matrix Method (TMM), Eigenmode Expansion Method (EEM), and Finite Integration Technique (FIT). This methods are presented with a self-written code for TMM, freeware CAvity Modeling FRamework (CAMFR) for EEM, and commercial software Microwave Studio (MWS) of CST for FIT method.

In chapter 3, the slow light line-defect waveguide is presented. An approach is discussed to achieve small group velocity with vanishing second and third order dispersion. An example of the waveguide is given with group velocity 0.02 speed of light on the bandwidth of approximately 1 THz. The group velocity reduction is explained through power flow redistribution.

In chapter 4, large second order dispersion is demonstrated near the anticrossing point in single and coupled line-defect waveguides. Theoretical estimations are given for maximal achievable dispersion. Quasi constant positive and negative dispersion is predicted in the order of 100ps/nm/mm on the bandwidth of 100GHz.

In chapter 5, an approach is developed to estimate the time delay of Bloch mode propagation in chirped periodical structures. The approach is demonstrated on high index contrast chirped Bragg mirrors and complex photonic crystal waveguide structures, including coupled waveguides and a slow light waveguide. It allows simple design of time delay and dispersion compensation waveguides in chirped PC structures.

In chapter 6, an approach is presented to couple light into a slow light mode of a PC line-defect waveguide. Two stage coupling is proposed, where strip waveguide mode is coupled to the "index guided" mode of the PC waveguide and the "index guided" mode is butt-coupled or adiabatically changed into a slow light mode. A comparison with one dimensional structure at the band edge is provided which demonstrates the advantage of the line-defect waveguides.

In chapter 7, characteristics of disordered Bragg stacks and line-defect waveguides are simulated. The backscattering effect on transmission and time delay is estimated. First, the reflection at a single defect is calculated and then the results are used to estimate reflection intensity in the disordered structure with statistical distribution of defects. The dependency of the backscattering intensity on the group velocity and disorder amplitude are investigated.

In chapter 8, the results of the previous chapters are summarized and the outlook for further investigations is given.

2. Background

The background information about PC line-defect waveguides and their simulations is presented. Three simulation approaches are described: Transfer Matrix Method (TMM), Eigenmode Expansion Method (EEM), and Finite Integration Technique (FIT). This methods are presented with a self-written code for TMM, freeware CAvity Modeling FRamework (CAMFR) for EEM, and commercial software Microwave Studio (MWS) of CST for FIT method.

2.1 Photonic crystal line-defect waveguides

Photonic crystal is a dielectric material or a set of different dielectric materials with periodical distribution of refractive index. An introduction to photonic crystal theory can be found in the book of Joannopoulos, Meade and Winn [36]. We will concentrate on the two dimensional triangular lattice photonic crystals with cylindrical air holes in silicon. The line-defect is obtained by leaving out a row of holes along the ΓK direction, which corresponds to the direction to the first nearest neighbor holes.

2.1.1 2D structure

The essential properties of the line-defect waveguide can be investigated on the 2D structure. In this case the third dimension is disregarded as if the photonic crystal is infinite in this direction. In Fig. 2.1 a schematic picture of a line defect is shown with one row of holes missing in the ΓK direction. Several parameters define the waveguide structure. Lattice constant a is equal to the distance between closest holes. W is the waveguide width, it is measured relative to a single row missing waveguide $W = a\sqrt{3}$. Radius of the holes is r. All the dimension parameters are usually normalized to the lattice constant. The structure can be scaled to operate at any required frequency by the adjustment of the lattice constant, as can be derived from scaling properties of Maxwell equations [36]. The refractive index of the silicon matrix is taken as 3.5.
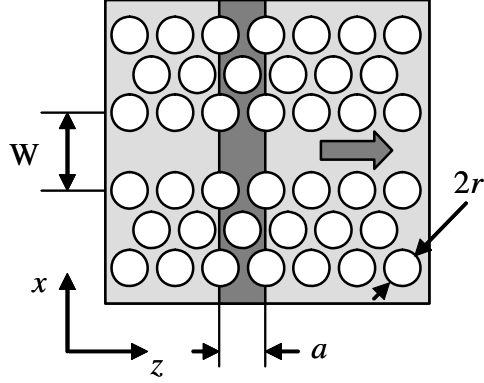
Fig. 2.1: Schematic picture of the W1 line-defect waveguide. A periodical unit is highlighted with dark grey color. The direction of mode propagation is shown with a grey arrow.

A triangular lattice of holes can have a complete band gap for light polarized in the plane of periodicity, which is usually defined as TE polarization. At this frequency range, called also as Photonic Band Gap (PBG), light is completely reflected and the photonic crystal behaves as an omnidirectional mirror. Thus line-defect waveguide effectively consist of two photonic crystal mirrors. If some modes can fit between these two mirrors then these modes propagate along the line-defect. The wider is the waveguide the larger is the number of guided modes. The dispersion relation of these modes can be found from an eigenmode problem, which can be defined for the periodical unit of the line-defect waveguide highlighted in the Fig. 2.1. Due to the Bloch theorem the electric field on the left and right side of this unit are related by the following equation:

$$\mathbf{E}(x, z + a) = \mathbf{E}(x, z)\,\mathbf{e}^{ika} \tag{2.1}$$

where k is the wavenumber. Applying different simulation approaches the eigenmodes can be found that fulfill the Maxwell equations and the Bloch boundary conditions. The eigenvalue of this problem is the frequency of the mode. Thus the dispersion relation can be obtained by scanning the eigenmode frequencies for different wave numbers. Such dispersion diagram, also called "band diagram", is presented in Fig. 2.2a. The frequencies and wavenumbers are presented in normalized units. Thus the band diagram is in this case lattice constant independent.

Fig. 2.2: (a) The band diagram of a 2D PC line-defect waveguide with one row of holes missing ($r = 0.3a$, W1, $n = 3.5$, TE polarization). (b) The amplitude of the magnetic field of mode v_2, mode v_1 and the odd mode (mode with a node on the line defining the lateral symmetry) are presented.

In Fig. 2.2 the modes of W1 waveguide are presented by thick lines. The radius of the holes is $r = 0.3a$, which is a typical value. Much larger holes are not possible due to the fact that the silicon walls between adjacent holes become to thin for lithography manufacturing. Thin dotted lines in Fig. 2.2a correspond to the modes outside PBG region, they are guided in the bulk PC and hence are not confined to the line defect. There are two continuous dispersion curves in the PBG region with different lateral symmetry of eigenmodes. The symmetry of eigenmodes is defined by its magnetic field in respect to the lateral plane in the waveguide center along z direction and normal to x direction (see Fig. 2.1). The amplitude of magnetic field is presented in Fig.2b. The odd mode has mode profile with a node in the middle of the line defect. The even mode has two different field distributions at the regions signed by v_1 and v_2. Though the line-defect modes are complicated they still remind the modes of a conventional dielectric waveguide, where v_2 looks like a fundamental mode, odd mode looks like a first mode and v_1 like a second mode. But due to the periodicity the modes are mixed and do not follow in the typical order.

The group velocity of the modes can be calculated as a dispersion relation derivative:

$$v_g = \frac{d\omega}{dk} \tag{2.2}$$

Thus the flatter the curve the smaller the group velocity. In the Fig. 2a the v_1 region corresponds to a very flat dispersion curve with very small group velocity. The investigation of this mode will be done in chapter 3.

2.1.2   2D slab structure

There are two ways to obtain line-defect modes in three dimensional structures. One of them is the complete three dimensional waveguide with a line defect [37][38]. But the manufacturing of such structures is still difficult from a technological point of view. Another approach is an extension of the 2D structure where total internal reflection is used to guide light in the vertical direction [6][23][24][30]. This 2D slab structure has properties very similar to the ideal 2D structure.
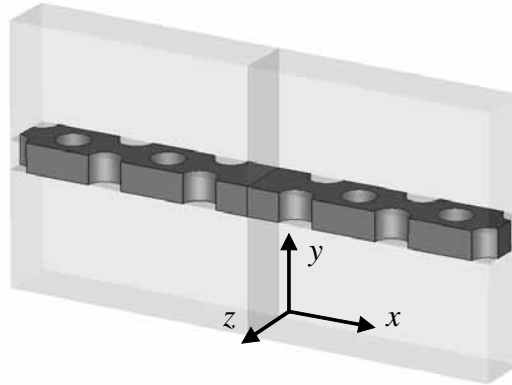
Fig. 2.3: A periodic unit of the 2D slab line-defect waveguide. Air cladding is added above and below slab. The slab has finite thickness $h = 0.5a$. The mode propagates along z axis.

In the Fig. 2.3 the slab structure is presented. The thickness of the slab is $h = 0.5a$. This a typical value for the high index contrast structures like silicon. At this value the slab is still monomode but at the same time light is strongly confined in the material. Below and above the slab sufficient air cladding is attached so that light can not tunnel out. The boundaries of the simulation volume should be sufficiently away from the waveguide center in x and y directions. In this case conductor boundary condition can be applied to these boundary planes. Along z direction Bloch boundary conditions are used similar to the discussed in the previous section. The band diagram of the presented structure is shown in Fig. 2.4a. The same odd and even modes are observed in the PBG region, though the PBG region is now at higher normalized frequencies. This can be explained by the fact that 2D slab modes penetrate into air claddings and thus propagate effectively in the medium with smaller refractive index. The main difference is the appearance of the radiation modes above the $\omega = k$ line, also called light line (presented with a grey line). The modes above the light line do not fulfill the total internal reflection condition and are scattered vertically. Thus only the modes below the light line are available in the 2D slab structure. The magnetic field amplitude of the υ_1 mode is presented in Fig. 2.4b. The field is taken on the xy planes and xz planes. On the xz plane the mode is very similar to the 2D mode presented in Fig. 2.2b.
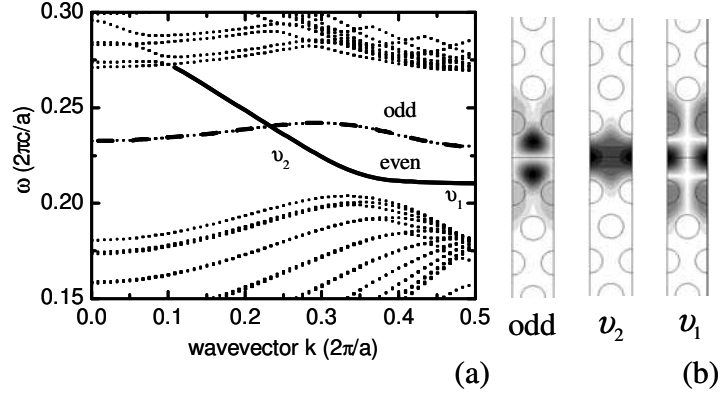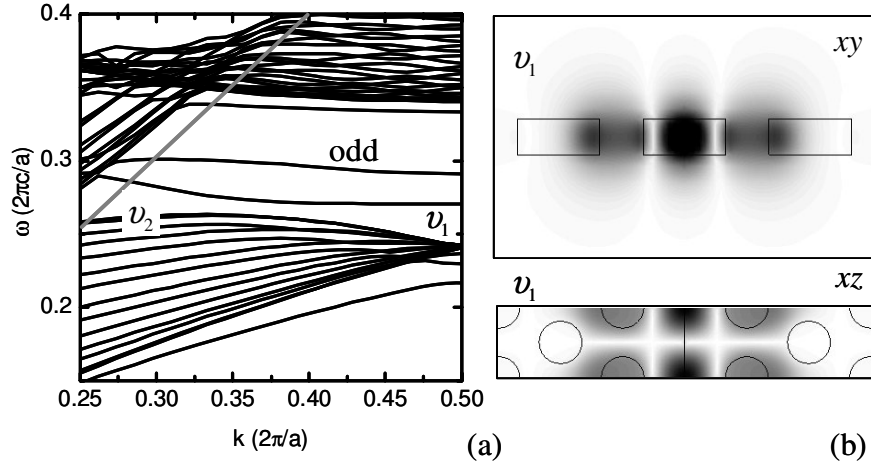
Fig. 2.4: (a) The band diagram of a 2D slab line-defect waveguide with one row of holes missing ($r = 0.3a$, W1, $n = 3.5$, $h = 0.5a$). The grey line corresponds to the light line of the slab (b) The amplitude of the magnetic field of the mode υ_1 is presented. The field is confined in the lateral and vertical directions.

2.2 Transfer Matrix Method

2.2.1 Approach

Transfer Matrix Method (TMM) is an approach to calculate transmission and reflection properties of 1D structures as a multiplication of transfer matrices. The TMM can be also extended to 2D and 3D structures but that will not be considered in this chapter. There are many possible ways to define transfer matrices, we will follow the approach presented in Ref [39]. The electric field at certain frequency ω in any layer inside the 1D structure can be considered as a sum of forward and backward propagating plane waves:

$$E(z) = E^+ e^{ikz} + E^- e^{-ikz} \tag{2.3}$$

where z is the propagation direction and k is the wavenumber. The forward component corresponds to E^+ taking the time factor as $e^{-i\omega t}$. The electric field sum can be presented in a vector form:

$$\mathbf{E} = \begin{pmatrix} E^+ \\ E^- \end{pmatrix} = \begin{pmatrix} f \\ b \end{pmatrix} \tag{2.4}$$

Then the propagation in the media can be described by a propagation matrix Π :

$$\mathbf{E}(z) = \Pi(-\delta)\mathbf{E}(z+\delta) \tag{2.5}$$

$$\Pi(\delta) = \begin{pmatrix} e^{ik\delta} & 0 \\ 0 & e^{-ik\delta} \end{pmatrix} \tag{2.6}$$

where δ is the propagation distance.

At the interface between two media the Fresnel transmission and reflection coefficients can be applied to connect fields on the left and right side of the interface. For the light falling from the left side the transmission t_{LR} and reflection r_{LR} coefficients are:

$$t_{LR} = \frac{2n_L}{n_L + n_R}, \; r_{LR} = \frac{n_L - n_R}{n_L + n_R}, \text{ where } 1 + r_{LR} = t_{LR}, \tag{2.7}$$

n_L and n_R are refraction indices of left and right media correspondingly. The interface transition can be also presented as a matrix $\Delta n_{L,R}$ that connects electric field on the left $\mathbf{E}_L$ and right $\mathbf{E}_R$ sides:

$$\mathbf{E}_L = \Delta n_{L,R} \cdot \mathbf{E}_R \tag{2.8}$$

$$\Delta n_{L,R} = \frac{1}{t_{LR}} \begin{pmatrix} 1 & r_{LR} \\ r_{LR} & 1 \end{pmatrix} \tag{2.9}$$

The field at the input of the structure with N layers can be thus connected to the field at the output by a following matrix multiplication:

$$\mathbf{E}_{in} = M\mathbf{E}_{out} \quad \text{with} \quad M = \Pi_1 \Delta n_{1,2} \Pi_2 \dots \Delta n_{N-2,N-1} \Pi_{N-1} \Delta n_{N-1,N} \Pi_N \tag{2.10}$$

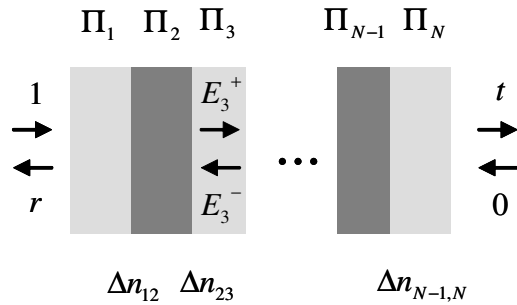*Fig. 2.5: Schematic presentation of the transfer matrix method. Every layer is presented by its propagation matrix Π and every transition between two layers is presented by matrix Δn. The structure is excited from the left side.*

The multilayer is also shown schematically in Fig. 2.5. If transfer matrix M is known, then the reflection r and transmission t coefficients can be found as follows:

$$M = \begin{pmatrix} M_{11} & M_{12} \\ M_{21} & M_{22} \end{pmatrix} \text{ and } \begin{pmatrix} 1 \\ r \end{pmatrix} = M \begin{pmatrix} t \\ 0 \end{pmatrix}, \text{ so}$$

$$t = M_{11}^{-1} \text{ and } r = M_{11}^{-1} M_{21} \tag{2.11}$$

On the other hand when reflection and transmission amplitudes are known the matrix coefficients M_{11} and M_{21} can be found. The invariance under time reversal can be used to define M_{12} and M_{22} [39] from the time reversed equations (2.11):

$$\begin{pmatrix} r* \\ 1 \end{pmatrix} = M \begin{pmatrix} 0 \\ t* \end{pmatrix}, \quad \text{so} \quad t* = M_{22}^{-1} \quad \text{and} \quad r* = M_{22}^{-1} M_{12}, \tag{2.12}$$

where $r*$ and $t*$ are complex conjugated reflection and transmission coefficients. Complex conjugation follows from time reversal of equation (2.3):

$$\left(E(z)e^{-i\omega t} \right)* = ((E^+)* e^{-ikz} + (E^-)* e^{+ikz})e^{i\omega t} \tag{2.13}$$

Thus the transfer matrix can be presented in general form as:

$$M = \begin{pmatrix} 1/t & r*/t* \\ r/t & 1/t* \end{pmatrix} \tag{2.14}$$

Accordingly, the reflection and transmission coefficients related to intensity are given by ratios of power flows:

$$R = \frac{n_1 \left| E_{in}^- \right|^2}{n_1 \left| E_{in}^+ \right|^2} = |r|^2, \; T = \frac{n_N \left| E_{out}^+ \right|^2}{n_1 \left| E_{in}^+ \right|^2} = \frac{n_N}{n_1} |t|^2, \text{ and } R+T=1 \tag{2.15}$$

It should be mentioned that transmission intensity is not just the transmission amplitude squared, but also multiplied by the refraction index of the medium. The determinant $\det(M)$ is equal to 1 only in the case when input and output media have the same refraction index. The phase information is contained in the reflection and transmission coefficients as follows:

$$t = |t|e^{i\varphi_t}, \; r = |r|e^{i\varphi_r} \tag{2.16}$$

Thus transmission and reflection amplitude and phase can be obtained for every frequency point.

2.2.2 Bloch modes

The periodical structure has eigenmode solutions, also called Bloch modes. This eigenmodes within the TMM approach can be presented as eigenvectors. The Bloch mode boundary condition (2.1) can be rewritten in a vector form:

$$\begin{pmatrix} f \\ b \end{pmatrix}_{z+a} = e^{ik_B a} \begin{pmatrix} f \\ b \end{pmatrix}_z \tag{2.17}$$

where k_B is the Bloch mode wavenumber. On the other hand, the periodical unit can be described by its transfer matrix M^a and the Bloch boundary condition leads to an eigenvalue problem:

$$e^{-ik_B a} \begin{pmatrix} f \\ b \end{pmatrix}_{z+a} = M^a \begin{pmatrix} f \\ b \end{pmatrix}_{z+a} \tag{2.18}$$

Taking into account that $\det(M^a) = 1$, the dispersion relation can be found [40]:

$$e^{-ik_B a} = \frac{1}{2}\left(M^a_{11} + M^a_{22}\right) \pm \sqrt{\frac{1}{4}\left(M^a_{11} + M^a_{22}\right)^2 - 1} \tag{2.19}$$

The frequency is contained in the propagation matrices Π. Two eigenvectors can be found from the equation (2.18) [40]:

$$\mathbf{E}^1_B = \begin{pmatrix} M^a_{12} \\ M^a_{11} - e^{-ik_B a} \end{pmatrix} \tag{2.20}$$

$$\mathbf{E}^2_B = \begin{pmatrix} M^a_{22} - e^{-ik_B a} \\ M^a_{21} \end{pmatrix} \tag{2.21}$$

They present forward and backward propagating Bloch modes:

$$\mathbf{E}^+_B = \begin{pmatrix} f \\ b \end{pmatrix}, \text{where } |f| > |b| \tag{2.22}$$

$$\mathbf{E}^-_B = \begin{pmatrix} b* \\ f* \end{pmatrix} \tag{2.23}$$

2.2.3 Bloch mode excitation, reflection and transmission

Bloch modes found in the previous section are the eigenmodes of the periodical stacks. They propagate in the ideal periodical structure without change and can be scattered at any periodicity fault. To investigate this scattering it is important to have a periodical stack with defect and absorbing boundary conditions at the input and output. The absorbing boundary in this case should absorb Bloch modes without reflection as if there is an infinite periodical stack attached to the boundary. This boundary condition can be obtained by considering excitation, reflection and transmission as Bloch modes:

$$1 \cdot \begin{pmatrix} f \\ b \end{pmatrix}_{in} + r_B \begin{pmatrix} b* \\ f* \end{pmatrix}_{in} = M \cdot t_B \begin{pmatrix} f \\ b \end{pmatrix}_{out} \tag{2.24}$$

where r_B and t_B are Bloch mode reflection and transmission coefficients. By solving the matrix equation these coefficients can be calculated:

$$r_B = \frac{f_{in}c_2 - b_{in}c_1}{f_{in} * c_1 - b_{in} * c_2} \tag{2.25}$$

$$t_B = \frac{|f_{in}|^2 - |b_{in}|^2}{f_{in} * c_1 - b_{in} * c_2} \tag{2.26}$$

where

$$\begin{pmatrix} c_1 \\ c_2 \end{pmatrix} = M \begin{pmatrix} f \\ b \end{pmatrix}_{out} \tag{2.27}$$

The intensity of the reflected and transmitted Bloch modes can be again found from the power flow ratios:

$$R_B = |r_B|^2 \left(\frac{n_1}{n_1}\right) \frac{|f_{in}|^2 - |b_{in}|^2}{|f_{in}|^2 - |b_{in}|^2} = |r_B|^2,$$

$$T_B = |t_B|^2 \left(\frac{n_N}{n_1}\right) \frac{|f_{out}|^2 - |b_{out}|^2}{|f_{in}|^2 - |b_{in}|^2}, \tag{2.28}$$

$$R_B + T_B = 1$$

where power flow in the backward direction is subtracted from the power flow in the forward direction. The slow light modes near band edge have very small group velocity due to the fact that forward and backward power flows are almost equal. Thus to transmit the same power flow the amplitude of the forward and backward plane waves should be very high. Again the amplitude and phase of the reflected and transmitted Bloch waves can obtained similar to equation (2.16)

2.3   Eigenmode Expansion Method

2.3.1   Approach

The eigenmode expansion method (EEM) is a method to calculate transmission and reflection properties of arbitrary structures presented as eigenmodes of input and output cross sections. Any structure can be considered as a sum of z-invariant layers which are stacked together. We will concentrate on 2D structures schematically presented in Fig. 2.6. Any section from 1 to N is invariant in z direction, thus they guide z-invariant eigenmodes that propagate undisturbed until they meet an interface to the next layer. The field excited from the left can be presented as a sum of eigenmodes in layer 1. The eigenmodes should be orthogonal to allow unambiguous representation.

They are obtained as solution of 1D eigenmode problem which can be solved with a TMM method. There is generally an infinite number of eigenmodes when modes with imaginary propagation constants are included. The number should be truncated at some point *Nm* to allow numerical implementation of the method. This truncation is possible because higher order modes have very high frequency of field oscillation along *x* axis and they have very small value of the overlap integral with the propagating field. At the same time these modes have large imaginary propagation constants, thus they decay substantially in the layer and do not propagate to the next layer.

The eigenmodes propagate in the layers with phase shifts corresponding to their propagation constants or decay if their propagation constants are imaginary. At the interface they excite reflection as eigenmodes propagating in opposite direction and transmission as eigenmodes of the adjacent layer. When eigenmodes are known the transmission and reflection coefficients can be found from overlap integrals [41].
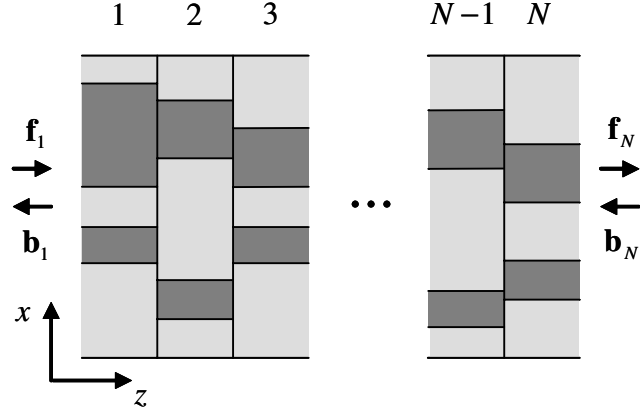
Fig. 2.6: Schematic presentation of the structure separated in the z-invariant layers. Different color corresponds to different dielectric constants. In every layer the field can be presented as a sum of forward and backward propagating eigenmodes.

The forward and backward propagating fields in every layer can be represented as vectors consisting of the amplitudes of eigenmodes:

$$\mathbf{f} = \begin{pmatrix} f_1 \\ f_2 \\ \dots \\ f_{Nm} \end{pmatrix}, \mathbf{b} = \begin{pmatrix} b_1 \\ b_2 \\ \dots \\ b_{Nm} \end{pmatrix} \tag{2.29}$$

Thus the transmission and reflection coefficients build transmission and reflection matrices $\mathbf{T}_{LR}$, $\mathbf{R}_{LR}$, $\mathbf{T}_{RL}$, $\mathbf{R}_{RL}$. They connect the forward and backward propagating fields in left and right layers. When all eigenmodes and interface matrices are know the transmission and reflection characteristics of the entire stack can be obtained. The TMM

method described in the previous chapter is a special case of the EEM with only one eigenmode in every layer.

The details of the eigenmode expansion implementation will not be discussed. This is described in the literature concerning simulation method CAvity Modeling FRamework (CAMFR) [41][42][43], which was also applied in this thesis. It should be mentioned that, contrary to the TMM method where transfer matrix is obtained as a multiplication of interface and propagation matrices, CAMFR makes use of the scattering matrix method which is calculated in a recursive form. The scattering matrix combines outgoing waves on both sides of the structure with input waves:

$$\begin{pmatrix} \mathbf{b}_1 \\ \mathbf{f}_N \end{pmatrix} = \mathbf{S} \begin{pmatrix} \mathbf{f}_1 \\ \mathbf{b}_N \end{pmatrix} = \begin{pmatrix} \mathbf{S}_{11} & \mathbf{S}_{12} \\ \mathbf{S}_{21} & \mathbf{S}_{22} \end{pmatrix} \begin{pmatrix} \mathbf{f}_1 \\ \mathbf{b}_N \end{pmatrix} \tag{2.30}$$

The cascade of two scattering matrices $\mathbf{S}_a$ and $\mathbf{S}_b$ is obtained not by multiplication but by the following procedure, as can be shown by direct multiplication of the matrix elements:

$$\mathbf{S}_{11}^{c} = \mathbf{S}_{11}^{a} + \mathbf{S}_{12}^{a}(\mathbf{I} - \mathbf{S}_{11}^{b}\mathbf{S}_{22}^{a})^{-1}\mathbf{S}_{11}^{b}\mathbf{S}_{21}^{a}$$

$$\mathbf{S}_{12}^{c} = \mathbf{S}_{12}^{a}(\mathbf{I} - \mathbf{S}_{11}^{b}\mathbf{S}_{22}^{a})^{-1}\mathbf{S}_{12}^{b}$$

$$\mathbf{S}_{21}^{c} = \mathbf{S}_{21}^{b}(\mathbf{I} - \mathbf{S}_{22}^{a}\mathbf{S}_{11}^{b})^{-1}\mathbf{S}_{21}^{a} \tag{2.31}$$

$$\mathbf{S}_{22}^{c} = \mathbf{S}_{22}^{b} + \mathbf{S}_{21}^{b}(\mathbf{I} - \mathbf{S}_{22}^{a}\mathbf{S}_{11}^{b})^{-1}\mathbf{S}_{22}^{a}\mathbf{S}_{12}^{b}$$

where $\mathbf{S}_c$ is the matrix of the cascaded structure and $\mathbf{I}$ is the unit matrix. The scattering matrix approach is more stable than the transfer matrix as discussed in Ref. [41]. When the scattering matrix is obtained the reflection and transmission matrices $\mathbf{T}_{1N}$, $\mathbf{R}_{1N}$, $\mathbf{T}_{N1}$, $\mathbf{R}_{N1}$ can be derived:

$$\mathbf{f}_N = \mathbf{T}_{1N}\mathbf{f}_1 + \mathbf{R}_{N1}\mathbf{b}_2 , \qquad \mathbf{b}_1 = \mathbf{R}_{1N}\mathbf{f}_1 + \mathbf{T}_{N1}\mathbf{b}_2 \tag{2.32}$$

They can be rewritten as a transfer matrix $\mathbf{M}$:

$$\begin{pmatrix} \mathbf{f} \\ \mathbf{b} \end{pmatrix}_1 = \mathbf{M} \begin{pmatrix} \mathbf{f} \\ \mathbf{b} \end{pmatrix}_N = \begin{pmatrix} \mathbf{T}_{1N}^{-1} & \mathbf{T}_{1N}^{-1}\mathbf{R}_{N1} \\ \mathbf{R}_{1N}\mathbf{T}_{1N}^{-1} & \mathbf{T}_{N1} - \mathbf{R}_{1N}\mathbf{T}_{1N}^{-1}\mathbf{R}_{N1} \end{pmatrix} \begin{pmatrix} \mathbf{f} \\ \mathbf{b} \end{pmatrix}_N \tag{2.33}$$

2.3.2 Bloch modes

The Bloch modes of the structure periodical in z direction can be found as a solution of the following eigenvalue problem:

$$\begin{pmatrix} \mathbf{f} \\ \mathbf{b} \end{pmatrix} = \mathbf{M}^a \cdot e^{ik_B a} \begin{pmatrix} \mathbf{f} \\ \mathbf{b} \end{pmatrix} \tag{2.34}$$

where $\mathbf{M}^a$ is the transfer matrix of the periodical unit and k_B is the propagation constant of the Bloch modes. The transfer matrix has dimensions $2Nm \times 2Nm$, thus $2Nm$ eigenmodes will be found. These eigenmodes can be separated in Nm forward

and *Nm* backward propagating modes, where direction is defined by the power flow of the Bloch modes. We will distinguish forward and backward propagating Bloch modes with sign "+" and "–". The field in any layer can be presented as a sum of Bloch modes. The Bloch modes amplitudes build also a vector which can be converted to the cross section eigenmode representation by a matrix transformation:

$$\begin{pmatrix} \mathbf{f} \\ \mathbf{b} \end{pmatrix} = \mathbf{G}_{BE} \begin{pmatrix} \mathbf{f} \\ \mathbf{b} \end{pmatrix}_B \tag{2.35}$$

where *B* stands for "Bloch" and $\mathbf{G}_{BE}$ consists of the Bloch modes obtained from the eigenvalue problem (2.34):

$$\mathbf{G}_{BE} = \left(\begin{pmatrix} \mathbf{f} \\ \mathbf{b} \end{pmatrix}_1^+ \begin{pmatrix} \mathbf{f} \\ \mathbf{b} \end{pmatrix}_2^+ \cdots \begin{pmatrix} \mathbf{f} \\ \mathbf{b} \end{pmatrix}_{Nm}^+ \begin{pmatrix} \mathbf{f} \\ \mathbf{b} \end{pmatrix}_1^- \begin{pmatrix} \mathbf{f} \\ \mathbf{b} \end{pmatrix}_2^- \cdots \begin{pmatrix} \mathbf{f} \\ \mathbf{b} \end{pmatrix}_{Nm}^- \right) = \begin{pmatrix} \mathbf{F}^+ & \mathbf{F}^- \\ \mathbf{B}^+ & \mathbf{B}^- \end{pmatrix} \tag{2.36}$$

2.3.3 Bloch mode excitation, reflection and transmission

Similar to the reasons discussed in TMM method an approach is required to excite Bloch modes and consider reflection and transmission as Bloch modes too. Equation (2.33) can be transformed to the Bloch mode representation at input and output with the help of equation (2.35):

$$\mathbf{G}_{BE}^{inp} \begin{pmatrix} \mathbf{f} \\ \mathbf{b} \end{pmatrix}_B^{inp} = \mathbf{M} \, \mathbf{G}_{BE}^{out} \begin{pmatrix} \mathbf{f} \\ \mathbf{b} \end{pmatrix}_B^{out} \tag{2.37}$$

In case of known amplitudes of excitation Bloch modes **i** the equation appears as follows:

$$\mathbf{G}_{BE}^{inp} \begin{pmatrix} \mathbf{i} \\ \mathbf{r} \end{pmatrix}_B = \mathbf{M} \, \mathbf{G}_{BE}^{out} \begin{pmatrix} \mathbf{t} \\ 0 \end{pmatrix}_B \tag{2.38}$$

There are all together *2Nm* unknowns in the reflection **r** and transmission **t** vectors which can be found with the *2Nm* equations in the matrix equation (2.38). Thus when matrix **M** is known any excitation and outcoupling scheme can be simulated without recalculation of the transfer matrix.

2.4 Finite Integration Technique

In this thesis the program "Microwave Studio" was used which was designed for microwave electromagnetic simulations and is based on the FIT method. The simulations at optical frequencies were possible due to the scalability of Maxwell equations [36]. This program is produced by the Computer Simulation Technology (CST) company and is commercially available. Many examples of the application of this software to photonic crystal problems can be found in the thesis of G. Boettger [44]

2.4.1   Approach

Finite Integration Technique (FIT) is a numerical method to simulate electromagnetic problems in time and frequency domain. The simulation volume is discretized with two orthogonal rectangular grids (see Fig. 2.7). A primary grid is used to calculate the electric voltages **e** and the magnetic fluxes **b**. The secondary or dual mesh is shifted by half the lattice vector and is used to calculate magnetic voltages **h** and dielectric fluxes **d**. The voltages are defined as line integrals on the edges of the grids, for example electric voltage $\mathbf{e}_i$ is calculated as $\int_L \mathbf{E}\, d\mathbf{r}_i$, and fluxes are defined as surface integrals on the corresponding facets, for example $\mathbf{b}_n = \iint_S \mathbf{B}\, d\mathbf{n}_n$, where $\mathbf{n}_n$ is the vector normal to the facet.
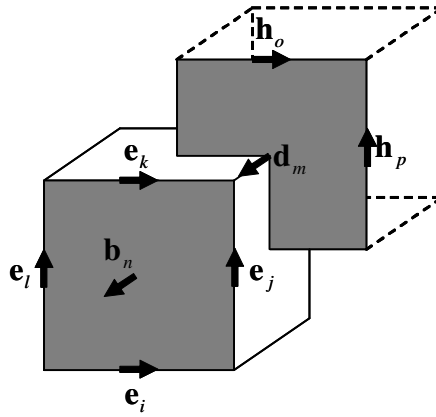
Fig. 2.7: The unit cells of the primary and secondary grids used for the discretization in FIT method. The electric voltages **e** *and magnetic fluxes* **b** *are defined on the edges and facets of the primary grid which is shown by solid lines. And magnetic voltages* **h** *and dielectric fluxes* **d** *are defined on the edges and facets of the secondary grid which is shown by dashed lines.*

The curls $\nabla \times$ and divergences ∇ operators in the Maxwell equations can be presented as matrix operators on the grid vectors. For example, a well known equation, a differential form of Faraday's law of induction:

$$\nabla \times \mathbf{E} = -\frac{\partial}{\partial t}\mathbf{B} \tag{2.39}$$

can be presented at the facet n (see Fig. 2.7) as:

$$e_i + e_j - e_k - e_l = -\frac{\partial}{\partial t}b_n \tag{2.40}$$

and in matrix form for the entire volume:

$$\mathbf{Ce} = -\dot{\mathbf{b}} \tag{2.41}$$

where **C** corresponds to the curl operator and contains only {-1,0,1} numbers. It defines for every facet in the structure the right order of the summation on the closed paths around the facets. The remaining three Maxwell equations can be presented in the corresponding way and all together they form the Maxwell Grid Equations (MGE) [44][45]:

$$\mathbf{S}\,\mathbf{b} = 0 \tag{2.42}$$

$$\mathbf{j} + \dot{\mathbf{d}} = \tilde{\mathbf{C}}\mathbf{h} \tag{2.43}$$

$$\tilde{\mathbf{S}}\,\mathbf{d} = \mathbf{q} \tag{2.44}$$

where **j** are the electric currents through facets and **q** are the electric charges in grid cells, **S** corresponds to the divergence operator and tilde sign "~" corresponds to the operators in the secondary grid. This grid equations should be supplemented by material equations which can be also presented in matrix form:

$$\mathbf{d} = \mathbf{D}_{\varepsilon}\mathbf{e} \tag{2.45}$$

$$\mathbf{b} = \mathbf{D}_{\mu}\mathbf{h} \tag{2.46}$$

$$\mathbf{j} = \mathbf{D}_{\sigma}\mathbf{e} + \mathbf{j}_{S} \tag{2.47}$$

where $\mathbf{D}_{\varepsilon}$, $\mathbf{D}_{\mu}$, $\mathbf{D}_{\sigma}$ correspond to the material permittivity, permeability and electric conductivity tensors, and $\mathbf{j}_{S}$ is the currents of the excitation sources.

2.4.2   Time domain simulations

The grid equations (2.41) and (2.43) contain time derivatives. When initial fields are specified the time evolution can be calculated via the so called leapfrog scheme. The time is discretized with intervals Δt and the fields are updated from previous magnetic fluxes and electric voltages which are shifted in time by $\Delta t / 2$. First, electric voltages are obtained at time step $n + 1/2$ from previous magnetic fluxes $\mathbf{b}^{n}$ and electric voltages $\mathbf{e}^{n-1/2}$:

$$\mathbf{e}^{n+1/2} = \mathbf{e}^{n-1/2} + \Delta t\,\mathbf{D}_{\varepsilon}^{-1}\left(\tilde{\mathbf{C}}\mathbf{D}_{\mu}^{-1}\mathbf{b}^{n} + \mathbf{j}_{S}^{n}\right) \tag{2.48}$$

And afterwards the magnetic fluxes are updated from $\mathbf{b}^{n}$ and $\mathbf{e}^{n+1/2}$:

$$\mathbf{b}^{n+1} = \mathbf{b}^{n} - \Delta t\,\mathbf{C}\mathbf{e}^{n+1/2} \tag{2.49}$$

These equations can be obtained from the MGEs as shown in [45]. The procedure can be repeated until the specified number of steps is reached, which is, for example, corresponds to the propagation time of the optical signal through the structure. From the grid vectors the magnetic and electric fields can be calculated at any time. Time dependences can be converted to frequency domain by Fourier transformation. Thus the complete spectral dependencies can be obtained within one simulation run.

18

2.4.3   Bloch modes

The Bloch modes of the periodical structure can be calculated with the eigenmode solver based on FIT method. The time derivatives can be eliminated from the Maxwell equations by considering the time harmonics $\exp(-i\omega t)$. Thus typical eigenmode equation is obtained:

$$\nabla \times \frac{1}{\mu} \nabla \times \mathbf{E} = \omega^2 \varepsilon \mathbf{E} \tag{2.50}$$

which can be presented in matrix form as:

$$\tilde{\mathbf{C}} \mathbf{D}_{\mu^{-1}} \mathbf{C} \mathbf{e} = \omega^2 \mathbf{D}_\varepsilon \mathbf{e} \tag{2.51}$$

The boundary conditions are directly implemented in the eigenmode problem. In case of Bloch mode calculations the Bloch boundary condition is defined (see (2.1)). The phase shift between two boundaries $\varphi = ka$ can be varied from 0 to π. The eigenfrequencies found for every phase shift build the dispersion relation of the Bloch modes which are presented, for example, in Fig. 2.2 and Fig. 2.4.

2.4.4   Bloch mode excitation, reflection and transmission

The direct Bloch mode excitation is not possible in the time domain FIT simulations. The FIT method is very similar to the propagation of electromagnetic fields in real structures. Thus to excite Bloch modes the couplers should be designed, similar to the real experiment, that converts plane waves or dielectric waveguide modes into Bloch modes of the periodical structure. The recalculations similar to presented in TMM and EEM methods are not possible in time domain method, because the excitation is not monochromatic.

3. Slow light waveguides with vanishing dispersion

Small group velocities near the band edge are observed in any waveguide with periodical corrugation, though the unavoidable group velocity dispersion is present. Thus optical signals, propagating through such waveguides will be strongly distorted. In this chapter we have examined PC line-defect waveguide modes and revealed the possibility to control the dispersion at small group velocities. Modes of photonic crystal line-defect waveguides can have a small group velocity even away from the Brillouin zone edge. This property can be explained by the strong interaction of the modes with the bulk PC. An anticrossing of "index guided" and "gap guided" modes should be taken into account. To control the dispersion the anticrossing point can be shifted by the change of the PC waveguide parameters. An example of a slow light waveguide is presented with vanishing second- and third order dispersion.

3.1 Introduction

PC waveguides were already proved to exhibit small group velocities down to $v_g = 0.02c$ [26]. We will mostly concentrate on obtaining a dispersionless waveguide, though this approach can be also used to achieve high quasi constant dispersion and therefore can be applied to compensation of the chromatic dispersion of optical fibers. There are also coupled cavities waveguides [29][46] where constant small group velocities are obtained. However, in slab waveguides [30] coupled cavity modes will lie above the light line and will thus exhibit high intrinsic losses. The coupled cavity waveguides are also more sensitive to disorder as discussed in chapter 7.

Silicon air-bridge structures with a triangular lattice of holes are considered, where a is the lattice constant, r is the radius of the holes, $n = 3.5$ is the slab refractive index, and $h = 0.5a$ is the thickness of the slab. The vertical component of the magnetic field is used to define the symmetry of the modes. Only vertically even TE-like modes are calculated, because they correspond to the fundamental slab mode and demonstrate photonic band gaps (PBGs) [30]. A line-defect waveguide is formed by leaving out a

row of holes in the ΓK direction and shifting the boundaries together. The width is defined as the distance between the hole centers on both side of the waveguide. It is measured in percentage of $W = \sqrt{3}a$.

3.2   Index guided and gap guide modes

The band diagram and field distribution of a 2D W1 waveguide are presented in Fig. 2.2. First, the modes at frequencies inside the PBG can be separated by their lateral symmetry of magnetic field (with respect to a plane along the propagation direction and vertical to the slab) to even and odd modes. The even mode of such waveguides can be categorized with respect to their field distribution as "index guided" v_2 or "gap guided" v_1 [6]. An index guided mode has its energy concentrated inside the defect and interacts only with the first row of holes adjacent to the defect. Its behavior can be simply represented by a dielectric waveguide with periodical corrugation [47]. As can be seen from Fig. 2.2b, a gap guided mode interacts with several rows of holes, thus it is dependent on the symmetry of the PC and its PBG. The names "index guided" and "gap guided" don't specify exactly the guidance mechanisms (in the PBG region all modes are gap guided) but mainly describe the resemblance in terms of the modal field distribution.

Any mode of the periodical waveguide generally shows a small group velocity near the band edge which eventually vanishes at the Brillouin zone edge. A simple parabolic approximation can be considered:

$$\omega \approx \left(\frac{\Delta k}{\alpha}\right)^2 + \omega_0 \tag{3.1}$$

where ω is the mode frequency, ω_0 is the mode frequency at the Brillouin zone edge, Δk is the wave vector difference to its value at the Brillouin zone edge, α is a function of the corrugation strength and depends mostly on the index contrast and the hole radii. The stronger the corrugation the flatter the mode becomes near the band edge. The first derivative over the wavevector is the group velocity:

$$v_g = \frac{d\omega}{dk} \sim \frac{\Delta k}{\alpha^2} \sim \frac{(\omega - \omega_0)^{1/2}}{\alpha} \tag{3.2}$$

the second derivative over the frequency is the dispersion:

$$D \sim \frac{d(1/v_g)}{d\omega} \sim \frac{\alpha}{(\omega - \omega_0)^{3/2}} \sim \frac{1}{\alpha^2 v_g^3} \tag{3.3}$$

So the stronger the corrugation the smaller is the dispersion at the same group velocity. In any case, the cubic dependency on the inverse group velocity makes the application of small group velocities difficult due to the large signal distortion.
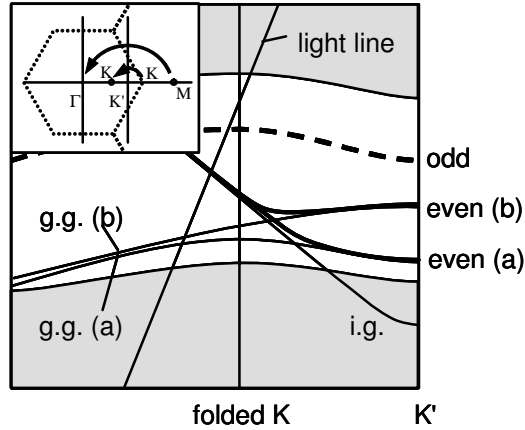
Fig. 3.1: Schematic band structure of a triangular lattice line-defect waveguide. Appearance of the folded K point is shown in the inset. The laterally odd mode has a negative slope between the folded K and K' points. The laterally even mode is formed as an anticrossing of index guided and gap guided modes. Two cases are possible: (a) the gap guided mode has a negative slope and the PC mode has a monotonous dependency; (b) the gap guided mode has positive slope and the PC mode can have a non-monotonous dependency with two wavevectors for one frequency. To be truly guided all modes should stay below the light line.

Gap guided modes of the PC line defect waveguide show a complicated behavior. Due to the introduction of the line-defect in the triangular lattice the symmetry is broken and the edge of the Brillouin zone is shifted to the K' point (see inset Fig. 3.1). Thus the M point is folded back to the Γ point and the K point appears as a folded K point between the Γ and K' points. Group velocity can vanish also at the folded K point. A laterally odd mode has a node in the center of the PC line-defect waveguide and a lot of its energy is located in the PC lattice. Thus this mode is similar to the folded bulk PC mode from K' to M points with a maximum at the folded K point. Between the folded K and K' points one observes negative group velocity (positive group velocity in the unfolded band diagram) and a point of zero dispersion. But a laterally odd mode is difficult to couple with a monomode dielectric waveguide due to the symmetry mismatch. Thus we will concentrate on laterally even modes.

3.3 Anticrossing point shift

There is an intrinsic interaction of even gap guided and index guided modes (Fig. 3.1) [6]. This interaction forms two supermodes, which are represented by the sum of gap guided and index guided modes in phase and in anti-phase. Due to the fast change of group velocity at the anticrossing point, the group velocity dispersion has a maximum there. This effect is very similar to the coupling of two dissimilar waveguides [48][49] except that here two modes from the same waveguide are coupled. The

anticrossing corrupts the flat region of the gap guided mode and should be avoided to achieve constant group velocity. One of the possibility is to shift the anticrossing point to the left of the band diagram. This was achieved by changing the waveguide width to W0.7. An example of the band diagram, group velocity and dispersion at the intersection point is shown in Fig. 3.2. The radius of the holes $r = 0.275a$ defines the value of the group velocity as will be discussed later in this chapter. At this waveguide width the anticrossing point with maximum dispersion is shifted to normalized frequency 0.313.
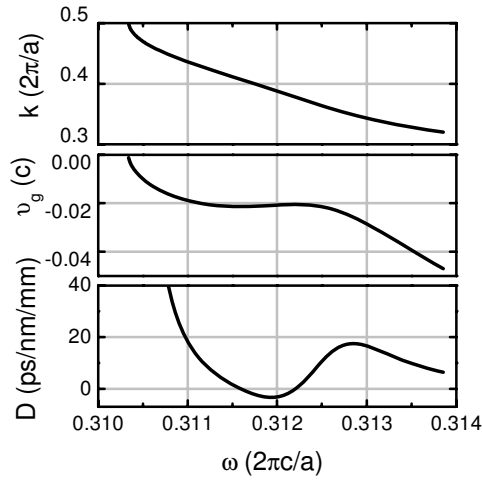

Fig. 3.2: The wave vector, group velocity and group velocity dispersion of the PC waveguide as functions of frequency ($r = 0.275a$, $h = 0.5a$, W0.7, air bridge $n = 3.5$). Normalized frequency is used, $a = 465\,nm$ corresponds approximately to 200 THz mode frequency (1500 nm wavelength). Group velocity $-0.02c$ has a bandwidth of constant value (approx. 1 THz), dispersion is almost zero throughout this bandwidth.

The anticrossing point shift can be explained by different sensitivity of the index guided and gap guided modes to waveguide width. A decrease of the waveguide width moves up both the gap guided and index guided modes in the band diagram (Fig. 3.3). However, the gap guided mode moves faster. This is similar to the modes of the mirror waveguide: the higher order modes are more sensitive to waveguide dimensions whereas the frequency of the fundamental mode approaches a constant value $\omega = nk$. Thus, the anticrossing point shifts to smaller wave numbers (Fig. 3.4). The gap guided mode alone would have a maximum of its group velocity somewhere between the folded K and K' points. In the W1 waveguide the anticrossing takes place before this maximum is achieved. By shifting the anticrossing point to the left a maximum of group velocity is obtained. The group velocity dispersion is zero there (see normalized frequency 0.312 in Fig. 3.2). The anticrossing can be adjusted in a way that even the third order dispersion is zero (approx. at W0.7) and thus the bandwidth of constant

group velocity is increased. To keep the group velocity in the 10% accuracy limits the deviation of the waveguide width should be not more than 0.01W what corresponds to the 8 nm precision in holes positioning.
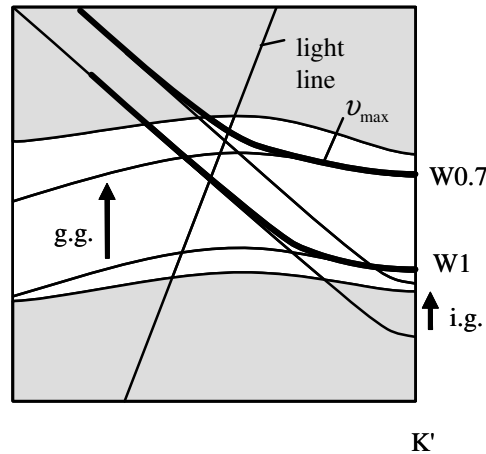
Fig. 3.3: Schematic band diagram of the W0.7 and W1 waveguides. The line-defect modes are shown with thick black lines. Thin black lines correspond to the imaginary index guided and gap guided modes taking part in the anticrossing process. The anticrossing point is shifted to the left and group velocity maximum is obtained in W0.7 waveguide.
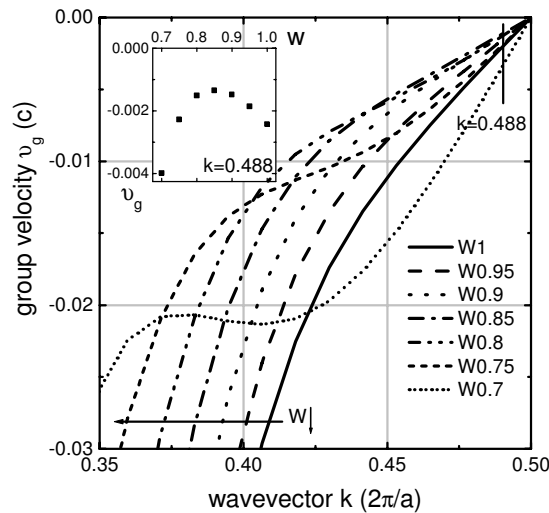
Fig. 3.4: Group velocity as a function of a wavenumber for $r = 0.275a$ with different waveguide widths. The inset shows group velocity at the $k = 0.488$ point, absolute value of group velocity has minimum at W0.85. The point of anticrossing with an index guided mode shifts gradually to the left with decreasing waveguide width. A bandwidth of constant group velocity is obtained at W0.7.

25

3.4   Group velocity variation

The group velocity of the gap guided mode is a function of structural parameters. It can even have different sign as shown in Fig. 3.1 by even.a and even.b modes. In the presented waveguide the folded branch of index guided mode has negative group velocity. Thus it is important to obtain negative group velocity of the gap guided mode too. Otherwise there exist two modes at one frequency what makes the coupling problematic. Here we return to the important issue of the PC symmetry. As was already discussed, the odd gap guided mode, which interacts strongly with the PC, has zero group velocity at the folded K point and a negative group velocity between the folded K and K' points. The even gap guided mode concentrates most of its energy in the unstructured part of the waveguide. The strength of the PC, namely the radius of the holes, becomes important. The weaker the PC the deeper the even gap guided mode penetrates into PC and the stronger it feels the 2D periodicity. Depending on the radii of the holes, the group velocity between folded K and K' points can change from positive to negative (Fig. 3.5). To manufacture a structure with a group velocity within 10% accuracy limits the radius of the holes can deviate not more than $0.005a$ what corresponds to approximately 2 nm.
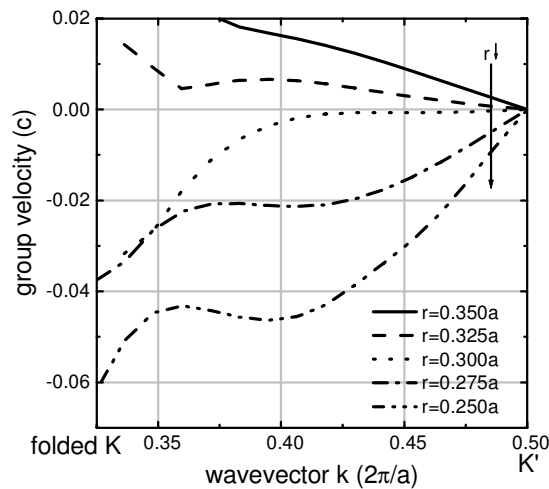
Fig. 3.5: Group velocity as a function of a wavevector for the even W0.7 waveguide mode with different radii of the holes. For large radii the gap guided mode has positive group velocity. As the radius decreases the group velocity becomes negative. A breaking point appears at $r = 0.3a$.

It is interesting to have a look at the energy flow of the gap guided and index guided modes [50]. As can be seen from Fig. 3.6 the gap guided mode has a power flow through adjacent holes opposite to the power flow in the line-defect. The group velocity is defined as

$$v_g = \frac{\int\limits_{-\infty}^{\infty} S_z\, dx}{(W_E + W_M)/a} \tag{3.4}$$

where S_z is the projection of Poynting vector on the z axis, W_E and W_M are the energies of the electric and magnetic field correspondingly in the unit cell of length a. Thus the group velocity is decreasing due to the partial opposite power flow. The power flow through adjacent holes changes with the radius of the holes (see Fig. 3.7). And the integral over the waveguide cross section defines the group velocity. In case of the waveguide with radius of the holes $0.35a$ the group velocity changes direction.
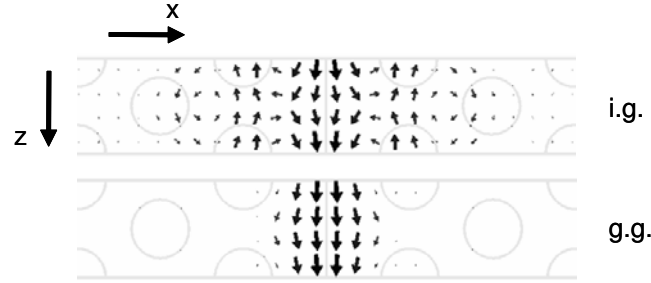
Fig. 3.6: Power flow distribution of index guided and gap guided modes in W1 waveguide at wavenumber $k = 0.3$ and $k = 0.4$.
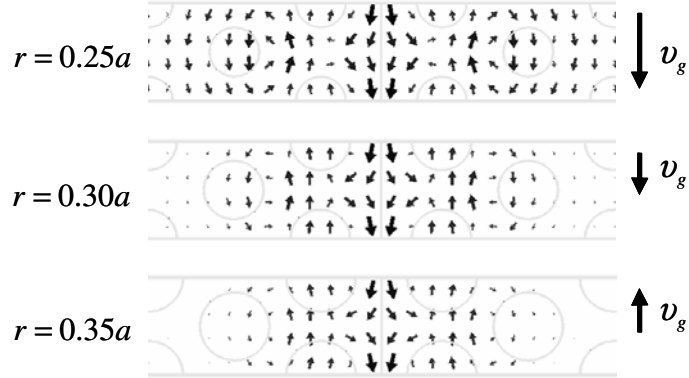
Fig. 3.7: Power flow distribution of gap guided modes in W0.7 waveguides with radius of the holes $0.25a$, $0.30a$, $0.35a$. The modes are calculated at normalized wavenumber $k = 0.4$. The penetration depth decreases with larger radius of the holes. The group velocity changes its direction. In the $0.35a$ waveguide the direction of group velocity is opposite to the power flow in the middle of the waveguide.

The depth of light penetration into the PC also changes with the waveguide width due to the shift in frequency. This also leads to the change of group velocity with waveguide width (see inset of Fig. 3.4). The change from W1 to W0.7 width shifts the

even modes from the lower to the upper edges of the PBG. Close to the PBG edges the penetration depth is large. Thus the gap guided modes follow the symmetry and exhibit quite large negative group velocity. In the middle of the PBG (W0.85) the penetration depth is smaller and the group velocity absolute value is decreasing.

3.5   Conclusion

In conclusion, we have thoroughly investigated the group velocity dispersion of PC line-defect waveguides in a triangular lattice slab. The importance of the PC 2D symmetry on the waveguide properties was shown. The influence of the penetration depth on the group velocity was demonstrated, where the penetration depth was controlled by the radii of the holes. It was shown that a simple PC waveguide with altered waveguide width W0.7 offers enough degrees of freedom to achieve a 1THz bandwidth of constant group velocity $0.02c$ with vanishing second- and third- order dispersion. We have introduced an approach to explain the dispersion relation of PC waveguide and how it can be modified. In this chapter we considered the most simple case, namely the width change, which is also favorable for manufacturing. To keep the group velocity in the 10% accuracy limits the deviation of the waveguide width should be not more than 8 nm and deviation of the radius of the holes not more than 2 nm.

The high index contrast of silicon to air material system and the vertical symmetry of the air-bridge structures are compulsory for the discussed applications. Only in this case the mode with constant group velocity stays below the light line throughout the bandwidth. The hole radii should be smaller than $0.3a$, otherwise a bistable mode is formed, which has two states at the same frequency: index-guide and gap guided. There will be a problem to couple from a conventional waveguide mode into the gap-guided mode, because due to the impedance match most of the energy will couple to the index guided mode. In the case of radii smaller than $0.3a$ the mode function has a monotonous behavior and adiabatic coupling can be applied (see [51] and chapter 6).

4. Waveguides with large positive and negative dispersion

A concept for dispersion compensation in transmission is proposed, based on modes anticrossing in photonic crystal line-defect waveguides. A quasi constant positive and negative dispersion is demonstrated in the order of 100ps/nm/mm on the bandwidth of 100GHz.

4.1 Introduction

Dispersion compensation plays a significant role in high-bit-rate long distance optical communication. Apart from conventional dispersion compensation fibers, which are several kilometers long, many concepts have been proposed and developed recently with their advantages and disadvantages. Chirped fiber Bragg gratings [52] operate in reflection and thus need 3dB couplers or circulators. All-pass filters [53][54] are tunable solutions, though obtained at a quite high complexity. Bragg gratings in transmission [55] and coupled cavities [29][46] operate at the band edge where higher order dispersion becomes a problem. Supermodes in coupled waveguides [48] or coupled fiber modes [49] can be used, but the achievable values of dispersion are not very high. Recently, chirped PC waveguides were investigated for their time delay properties [56][28]. Such waveguides can also be applied for dispersion compensation, where a single waveguide operates in reflection and coupled waveguides in transmission.

The applicability of uniform PC line-defect waveguides to chromatic dispersion compensation is investigated here, where the accumulated second order dispersion is simply scaled with length. In section 4.2 we consider two possible ways to achieve a high second order dispersion. For a device of a one centimeter length which addresses a single channel of the WDM scheme, dispersion at the anticrossing point is shown to have superior properties in comparison to dispersion at the band edge. Two concepts are proposed. First of them is described in section 4.3 and utilizes a single PC waveguide

where the mode in the PBG region is optimized to show a maximum of group velocity dispersion. Section 4.4 is devoted to the second concept were two coupled PC waveguides are used. Section 4.5 concludes the paper with the discussion of the proposed concepts.

4.2   Theoretical limits and approximations

4.2.1   Group velocity dispersion

Dispersion can be presented as a time delay change $\Delta\tau$ over a wavelength (frequency) change $\Delta\lambda$ ($\Delta\omega$). The time delay is proportional to the length and inverse proportional to the group velocity, so it is more convenient to consider dispersion per unit length:

$$D = \frac{1}{L}\frac{\Delta\tau}{\Delta\lambda} = \frac{1}{\Delta\lambda}\left(\frac{1}{v_2} - \frac{1}{v_1}\right) \tag{4.1}$$

where L is the length, v_1 and v_2 are the group velocities at λ_1 and λ_2, where $\lambda_2 - \lambda_1 = \Delta\lambda$. To achieve high values of dispersion we need a rapid change of the group velocity in the bandwidth of one channel. The largest possible value the group velocity can take is limited by the speed of light divided by the refraction index. At the same time the smallest group velocity can be arbitrary decreased in the periodical structures. When v_2 is much smaller than v_1, the dispersion is determined by the smallest group velocity:

$$D \approx \frac{1}{\Delta\lambda}\left(\frac{1}{v_2}\right) \tag{4.2}$$

The bandwidth of interest is 0.75 nm (100 GHz), which corresponds to one WDM channel, and a feasible group velocity limit is around $0.01c$ speed of light [6]. With such parameters we obtain 400 ps/nm/mm dispersion, where approximately 5mm of such negative dispersion will compensate for the propagation in the 100 km long fiber. Negative dispersion is needed for compensation, thus group velocity should decrease with decreasing wavelength (increasing frequency).

4.2.2   Dispersion at the band edge

Modes of any periodical structure generally have small group velocities near the band edge which eventually vanish at the Brillouin zone edge. A simple parabolic approximation can be considered (see (3.1)). It follows from equation (3.3) that dispersion is strongly frequency dependent. The dispersion change ΔD across the bandwidth of one channel should be taken into account. This effect is due to the third order dispersion, which can be expressed with group velocity and dispersion:

$$\frac{dD}{d\omega} = \frac{2\pi c}{\lambda^2} \frac{(-12)}{\alpha^4 v_g^5} = \frac{\lambda^2}{2\pi c}(-3)v_g D^2 \qquad (4.3)$$

$$\frac{\Delta D}{D} \approx \frac{dD}{d\omega}\frac{\Delta\omega}{D} = \frac{\lambda^2}{2\pi c}(-3)v_g D \Delta\omega \qquad (4.4)$$

The relative change of the dispersion should be small to avoid signal distortion, ratio $\Delta D / D \approx 0.25$ can be taken as an acceptable value [55]:

$$D \approx \frac{0.25}{3} \frac{1}{\Delta\lambda}\left(\frac{1}{v_g}\right) \qquad (4.5)$$

For the bandwidth $\Delta\lambda = 0.75$ nm and group velocity $0.01c$ we get a maximum tolerable value of dispersion around 40 ps/nm/mm. This value is much smaller than the theoretical limit (4.2). From this analysis we can conclude that any concept of dispersion compensation at the band edge will incur such problems and. A higher relative change of dispersion will inadvertently lead to strong pulse distortion.

4.2.3 Dispersion at the anticrossing point

Two originally isolated modes form two supermodes when interaction between them is allowed. The dispersion relation of these supermodes has an anticrossing behavior at the point where original dispersion curves intersect. If two original modes have a different sign of group velocities then a local band gap is formed and the behavior of the dispersion as derived for the band edge can then be observed in the vicinity of the anticrossing point. If the two original modes have different group velocities of the same sign, then each of the supermodes display a strong change of group velocity near the anticrossing point with a dispersion maximum exactly at the anticrossing. Applying the concepts of [48] from conventional waveguide modes to PC defect modes:

$$D = \frac{2\pi c}{\lambda^2} \frac{1}{2\delta\omega}\left(\frac{1}{v_1} - \frac{1}{v_2}\right)(\tilde{\omega}^2 + 1)^{-3/2} \qquad (4.6)$$

$$\delta\omega = 2\chi\left(\frac{1}{v_1} - \frac{1}{v_2}\right)^{-1} \qquad (4.7)$$

$$\tilde{\omega} = (\omega - \omega_0)/\delta\omega \qquad (4.8)$$

where $\tilde{\omega}$ is the normalized frequency, $\delta\omega$ is the characteristic bandwidth and χ is the coupling constant, v_1 and v_2 are group velocities of the original modes taking part in anticrossing. Taking into account 25% dispersion change on the bandwidth of interest we come to following estimation:

$$D \approx 0.46 \frac{1}{\Delta \lambda} \left(\frac{1}{v_g} \right) \qquad (4.9)$$

Dispersion is approximately 6 times higher than the one achievable at the band edge (4.5). For the same bandwidth $\Delta \lambda = 0.75$ nm and group velocity $0.01c$ dispersion is around 200 ps/nm/mm. This value of negative dispersion would allow to compensate the total chromatic dispersion of 100km of an optical single mode fiber within a device length of 10 mm.

4.3   Coupled modes in single PC waveguide

A typical band diagram of TE modes in the 2D PC with line-defect is presented in Fig. 2.2. The index guided mode at small frequencies is guided due to the index contrast, it is folded back into the first Brillouin zone due to the periodicity in the propagation direction. The index guided mode has most of its energy concentrated in the waveguide. The gap guided mode extends deeper into PC. It can propagate at much smaller group velocities as compared to the index guided mode as was investigated in chapter 3. The gap guided mode itself can have a large second order dispersion near band edge but with unavoidable third order dispersion as discussed in the previous section. The anticrossing point on the other hand allows to obtain a dispersion maximum with zero third order dispersion, thus a large and constant dispersion over the single channel bandwidth. The following concept relates to the coupled waveguides approach [49], however, in our case, instead of two modes of different waveguides two modes of the same waveguide are coupled.

In the W1 waveguide the anticrossing occurs close to the Brillouin zone edge, there is no sharp change of group velocity and thus no distinct dispersion maximum is observed. Decreasing the waveguide width moves both the index guided and the gap guided modes upwards but the gap guided mode moves faster and thus anticrossing point shifts to the smaller wavenumbers. A W0.75 waveguide shows a substantial dispersion maximum as depicted in Fig. 4.1. The bandwidth can be easily estimated from the normalized frequency bandwidth, taking into account that $\Delta \lambda / \lambda_0 = -\Delta \omega / \omega_0$ and $\Delta \lambda / \lambda_0 = 0.75 / 1500$. The minimum group velocity is $0.01c$, but the bandwidth is 3 times larger ($\Delta \omega / \omega_0 \approx 1/600$), thus the dispersion values are smaller than estimated. The bandwidth is a function of the coupling constant which, in our case, cannot be changed independently from group velocity of the gap guided mode.

Fig. 4.1: The wave vector, group velocity and group velocity dispersion of the PC waveguide as functions of frequency ($a = 360\,nm$, $r = 0.3a$, W0.75, $n = 3.5$, TE polarization). The structure is presented in the inset. Dispersion has a maximum of 55 ps/nm/mm at the normalized frequency $\omega \approx 0.2504$. Dispersion stays within 25% of the maximum value on the bandwidth of 300GHz.

The extra bandwidth of the previous structure can be used to increase dispersion. This can be achieved in a waveguide with smaller group velocity of the gap guided mode. The gap guided mode is very sensitive to the parameters of the waveguide. It penetrates into bulk PC deeper than index guided mode. Thus changing the distance between the row of holes adjacent to the waveguide and the row next to it, as shown schematically below the wavenumber graph in Fig. 4.2, the gap guided mode can be altered without significant shift of the index guided mode. In Fig. 4.2 the characteristics of the waveguide are shown, where the distance between second rows of holes is changed from W1.75 to W1.72. The gap guided mode is pushed to higher frequencies, its group velocity decreases to $0.005c$ and the bandwidth of the anticrossing range becomes two times smaller, however, still large enough. Thus the dispersion maximum is approximately 4 times larger (230 ps/nm/mm).

Unfortunately the sign of the dispersion is positive. To obtain the negative sign the supermode should be used where index guided and gap guided modes interact in anti-phase (anti-symmetric supermode). The gap guided mode has negative group velocity only between 0.33 and 0.50 normalized wavenumbers. In W0.75 waveguide anticrossing takes place near to the $k = 0.33$. The anticrossing point should be shifted

closer to the Brillouin zone edge, but in this case the anti-symmetric supermode is pushed out of the PBG region. More freedom to shift the anti crossing point is available in the coupled waveguides system as will be discussed in the next section.
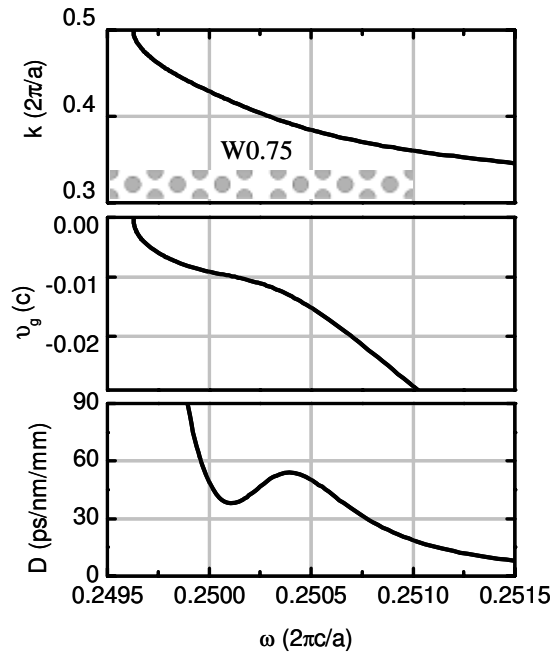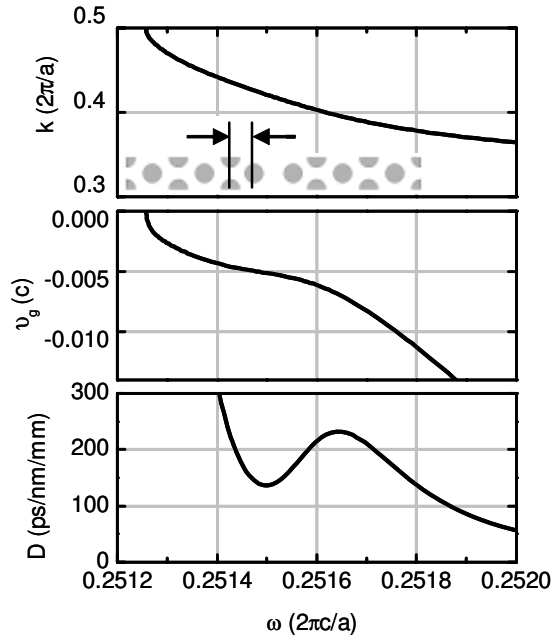

Fig. 4.2: The wave vector, group velocity and group velocity dispersion of the PC waveguide as functions of frequency ($a = 360\,nm$, $r = 0.3a$, first row W0.75, second row W1.72, $n = 3.5$, TE polarization). The distance between first and second rows of holes is changed (see schematic figure below the wavenumber graph). Dispersion has a maximum of 230 ps/nm/mm at the normalized frequency $\omega \approx 0.2516$. Dispersion stays within 25% of the maximum value on the bandwidth of 150 GHz.

4.4   Coupled PC waveguides

Dispersion compensation in coupled conventional dielectric waveguides was already investigated [48]. Two waveguides are coupled with different group velocities of guided modes. Two supermodes are formed at the anticrossing point, which consist of initial waveguide modes interacting in phase and in antiphase. These modes will be referred as symmetric and antisymmetric correspondingly. The symmetric mode shows a maximum of positive dispersion and the antisymmetric mode a maximum of negative dispersion. Maximum dispersion is inverse proportional to the coupling constant (4.6)(4.7) which exponentially decreases with distance between two waveguides. The bandwidth of the quasi constant dispersion is proportional to the coupling constant. Thus by taking the waveguides apart the dispersion maximum is increased and the bandwidth is decreased. But the inverse group velocity difference between two

34

dielectric waveguides cannot exceed certain values, because minimal group velocity is limited by approximately $c/3.5$, where 3.5 is the maximum refractive index available. For the bandwidth of 100GHz dispersion values for conventional waveguides stay well below 10ps/nm/mm. In contrast to conventional waveguides, PC waveguides can be designed to have very small group velocities, what allows to achieve much higher dispersion values.

In the Fig. 4.3 characteristics of the coupled PC waveguides are presented. Two waveguides of different waveguide widths are coupled. W0.75 waveguide at the operation frequency exhibits an even mode with very small group velocity and W047 waveguide has even mode with moderate group velocity. Coupling strength is controlled by the number of rows between two waveguides. In the presented example, a high negative dispersion is obtained (-150ps/nm/mm) on the bandwidth of 100GHz. By controlling the group velocities and the coupling strength arbitrary dispersion values and bandwidths can be obtained, limited only by the estimation (4.9).
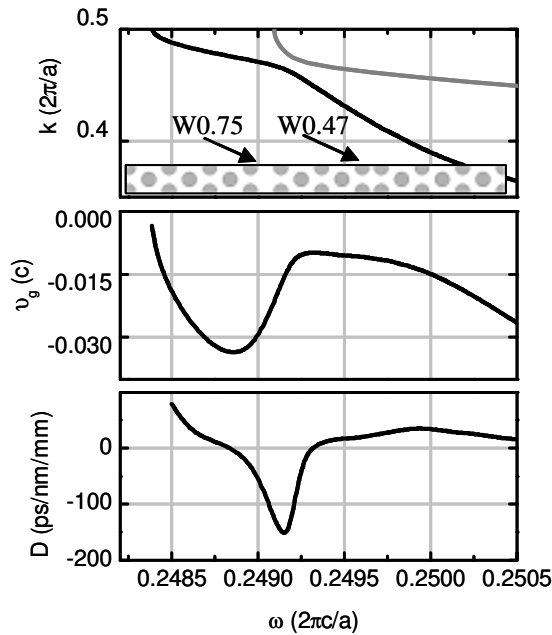
Fig. 4.3: The wave vector, group velocity and group velocity dispersion of the anti-symmetric supermode in the PC coupled waveguides system as functions of frequency ($a = 360\,nm$, $r = 0.3a$, W0.75 and W0.47, $n = 3.5$, TE polarization). The structure is presented in the inset, 5 rows of holes separate the coupled waveguides. The symmetric supermode is shown with the gray line. Dispersion has a maximum of -150 ps/nm/mm at the normalized frequency $\omega \approx 0.2492$. Dispersion stays within 25% of the maximum value on the bandwidth of 100GHz.

The main disadvantage of the coupled waveguides is the existence of both symmetric and anti-symmetric supermodes. There is a problem of coupling to the supermode of opposite symmetry. In [48] a special detuned coupler is applied which splits the energy equally between two waveguides and excites only the anti-symmetric supermode. This detuned coupler can be adjusted only for one frequency and will not work properly for other frequencies, unless additional limitations on the bandwidth are made. This fact makes the application of such a coupler not useful especially for PC waveguides where modes are very different even for a narrow bandwidth of 100 GHz. Adiabatic coupling can be used similarly to the one used for conventional coupled waveguides [57]. The outline for the coupler will look as follows. First, adiabatic coupling is used from the dielectric waveguide to excite light in W0.47 waveguide. Then, parallel to the W0.47 waveguide, the W0.7 waveguide is introduced, which has an anticrossing point at higher frequencies. The W0.7 waveguide can be gradually changed to W0.75 waveguide. It can be shown that the energy from W0.47 waveguide will be adiabatically transformed into anti-symmetric supermode.

4.5   Discussion and Conclusion

All effects discussed in this chapter occur due to the 2D periodicity of the PC. Thus 2D calculation are sufficient to show the validity of the approach. The extension to 2D PC slab structures which have to be treated as 3D volumes will shift the characteristics but will not change the concept. The only issue to be taken into account is the operation below the light line. To insure this the air-bridge concept should be used with air cladding on both sides of the slab waveguide (for example [6]). In such a structure there is enough space below the light line to adjust the anticrossing, still avoiding the lossy regime in the light cone . The mode will be strongly confined in the vertical direction and coupling loss is expected to be influenced mostly by the mode mismatch in the horizontal plane. In other words, the mode mismatch in the vertical direction will be much smaller compared to the mode mismatch in the lateral direction. A variation of the core thickness in this case can be used to shift the operational frequency but it doesn't influence the anticrossing behavior.

The modes anticrossing has been proven to have higher quasi-constant dispersion in comparison to the dispersion at the band edge. On the other hand dispersion at the band edge can be easily tuned by changing one of the PC waveguide parameters. An index change with temperature or carrier injection in silicon [31][32] will shift the band and thus will change the dispersion value. In case of anticrossing any change shifts the maximum from the frequency of operation. To change the dispersion value at least two tunable parameters are needed: one to change the dispersion value and another to shift the maximum back to the operational frequency.

We have demonstrated that a single line defect waveguide in the triangular lattice PC can have very high values of quasi-constant dispersion (230 ps/nm/mm for 150GHz bandwidth was shown). This dispersion is obtained at the anticrossing point of

index guided and gap guided modes. Unfortunately, there is no straightforward solution to obtain negative dispersion, because the anticrossing point cannot be arbitrarily shifted in a single waveguide and every parameter influences both index guided and gap guide modes. More freedom to adjust the anticrossing point is obtained in the coupled PC waveguides system, though at the cost of increased complexity. A high negative dispersion was shown (-150 ps/nm/mm).

5. Linearly chirped waveguides

The Bloch mode propagation through the chirped periodical structure is defined by its local dispersion relation. In a slowly varying structure its time delay is the integral of the local inverse group velocity along the propagation direction. The integration can be strongly simplified for linearly chirped structures if the assumption is made that the local dispersion relation is just a scaled and shifted version of the dispersion relation at the input. This assumption leads to exact solutions for the structures with locally uniaxial deformation and provides a good approximation for arbitrary structures with small chirps. The approach is demonstrated for high index contrast chirped Bragg mirrors and complex photonic crystal waveguide structures, including coupled waveguides and a slow group velocity waveguide.

5.1 Introduction

Chirped one-dimensional periodical structures like Fiber Bragg Gratings (FBGs) [52] and Bragg mirrors [58][59] are applied for dispersion compensation of optical signals. This devices operate usually in reflection so as to use nonminimum phase response of the optical filters [60]. One-dimensional filters in transmission have minimum phase response and the dispersion is usually achieved only near the edge of transmission band, where dispersion is highly nonlinear [55]. Recently, chirped PC structures have been introduced [56][28] were orders of magnitude size reduction can be expected in comparison to chirped FBGs. Taking into account additional flexibility as for example coupled waveguides [61][62][63][64], the chirped structures can be also designed to operate in transmission [28][8].

The conventional approach to chirped periodical structures involves the coupled mode theory [65][40]. It provides excellent results for low index contrast structures like silica based FBGs [52]. But it needs some nontrivial adjustments of the detuning parameters and coupling constants in case of high index contrast Bragg mirrors [59][66][67][68]. It is also difficult to extend for more complex structures like PC line

defect waveguides. A more consistent approach probably would be a Bloch mode description, which uses the eigenmode propagating in a periodical structure. This Bloch mode approach was already introduced for the explanation of light propagation in uniform [19] and non-uniform PC structures[69][51].

In this chapter a simplified approach is outlined to predict the time delay and pulse propagation in the slowly varying linearly chirped PC structures. As it was already discussed in [69] the Bloch mode propagates in every intermediate point of the chirped structure with a local group velocity, that can be defined from the local band diagram. The time delay in this case can be estimated as a path integral of inverse group velocity along the propagation direction. We consider only certain changes of the local band diagram, which allow direct analytical integration. These are linear scaling (proportional change of wavevector and frequency) and frequency shift. It is, thus, straightforward to predict time delay properties of the slowly varying chirped structure from the band diagram calculations without any limitations on its complexity. This approach provides exact solutions for the case of uniaxial deformation, due to scalability of Maxwell equations, and can be also used as an approximation for small chirps.

In section 5.2 we present the approach, discussing its main difference to the coupled mode theory, its approximations and limitations. A one dimensional example of a chirped Bragg grating is given in section 5.3 with a comparison to simulation results obtained with transfer matrix method (TMM). In section 5.4 the approach is applied to a rather complex chirped structure of coupled PC waveguides. An explanation is given for the pulse propagation observed with the time domain simulation in [28]. In section 5.5 we discuss the possible application of chirped small group velocity waveguides to dispersion compensation. Orders of magnitude size reduction is expected compared to the conventional chirped FBGs. The results are summarized in section 5.6.

5.2   Approach

We consider structures, that have periodical modulations of the refractive index in the direction of propagation. This can be a one dimensional Bragg grating or a line defect in two and three dimensional PCs. The chirp can be obtained by the gradual change of structural parameters [56],[70]. Examples of one and two dimensional structures are given in Fig. 5.1. In the Bragg stack both the lattice constant and the thickness of the high index layer are changed, in the PC line-defect waveguide the waveguide width is changed. Different wavelengths are thus reflected at the different locations within the chirped structure, producing a frequency dependent time delay.
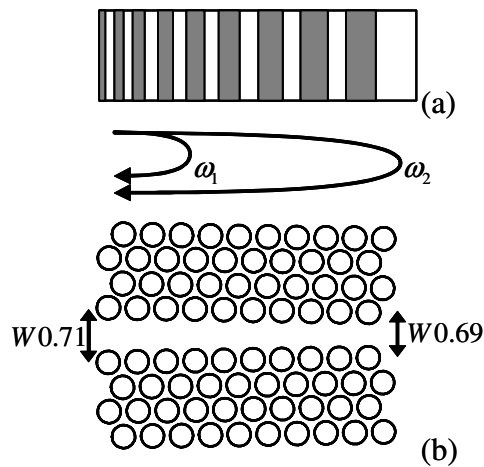
Fig. 5.1: Two examples of chirped periodical structures: (a) a Bragg stack with the increasing lattice parameter and (b) a PC line-defect waveguide with decreasing waveguide width. Different frequencies are reflected at different positions in the chirped structure.

5.2.1 Bloch modes propagation versus coupled modes equations

The usual approach to the chirped periodical structure is the coupled mode theory [65][40]. Two modes are considered with coupling due to the modulation of the index profile. The strongest coupling is observed when the half wavelength of the light equals the lattice constant of the periodical structure. This method is very flexible what concerns the chirp profiles and apodizations. In some cases even useful analytical solutions can be obtained. But this approach originally uses the assumption of low index contrast, where approximation of two coupled, however, unchanged modes is acceptable. In the standard coupled mode theory the coupling coefficient is constant and is determined by the first Fourier coefficient of the periodic refractive index function. In the case of a strong modulation the coupled mode approximation basically does not apply. But the mathematical similarity between the exact analytical solution for the Bragg stack and solution of coupled mode equations can be used to redefine the coupling constant and the detuning parameter to account for the strong index contrast [66][68]. This new parameters can be used afterwards in the calculation of chirped structures [59][67].

A completely different approach to the problem is provided with the eigenmodes of the periodical structure. These eigenmodes, also called as Bloch modes, appear as solutions of Maxwell equations with Bloch periodical boundary conditions, where the wavevector defines the phase shift between the Bloch boundaries and the eigenvalue gives the frequency of the mode [40]. As soon as excited in the lossless media the Bloch wave propagates without change through the unperturbated periodical structure [19]. Thus, propagation of light through any periodical structure is split into the plane wave to Bloch waves and vice versa coupling at the interfaces and the Bloch wave

propagation between them. The reflection at the interfaces can be calculated separately. The transmission characteristics in this case will be modified by the interference between the light reflected at the input and inside the chirped structure [71]. To avoid this interference the reflection should be as small as possible, what can be achieved, for example, by adiabatic coupling [51] as is presented in chapter 6. We should mention from the beginning that the goal of PC structures should be the separation of input and output channels. This will make the reflection less a problem due to the fact that the wave should be twice reflected to interfere with the output signal.

5.2.2 Band diagram approximation

We would like to propose a simple model of light propagation in a slowly varying chirped structure, that at the same time accounts for complicated dispersion relations of PC waveguides. It can be derived from the Hamiltonian optics approach to nonuniform photonic crystals developed in [69]. We will not consider the complete Hamiltonian formalism and will show a simple derivation of the time delay in a chirped periodical structure. We start from the Bloch wave already in the periodical structure thus leaving the plane to Bloch conversion to a separate discussion. The propagation of this Bloch wave through the slowly varying chirped structure can be described as a gradual transformation of the Bloch mode, following the adiabatic theorem [51]. Backscattering and possible scattering in the cladding are neglected in this case. In reality the first one leads to the appearance of ripples on the time delay function and the second increases the losses.

In every point there is an "instantaneous" periodical structure [51] and from the band diagram of this structure the wave vector can be found. The local wave vector of the mode with frequency ω_0 can be written as $k(\omega_0, z)$, where z is the direction of propagation. Thus the phase shift for the frequency ω_0 at any position in the structure can be defined as:

$$\varphi(\omega_0, z) = \int_0^z k(\omega_0, z)\, dz \tag{5.1}$$

The phase shift of an arbitrary structure can be found when all intermediate band diagrams are known. We would like to consider a special case of k functions. It is known that Maxwell equations are scalable, thus if all geometrical parameters of the periodical structure are defined relative to the lattice constant a then the band diagram is just scaled with relative change of lattice parameter [36]. The relative change parameter is defined as

$$\alpha(z) = \frac{a(z)}{a_0} \tag{5.2}$$

where a_0 is the lattice constant at the input. In normalized coordinates

$$\omega_{norm} = (\omega a)/(2\pi c) \tag{5.3}$$

$$k_{norm} = (k\,a)/(2\pi) \tag{5.4}$$

the band diagram $\omega_{norm}(k_{norm})$ stays the same and the normalized frequency changes with z. Due to the scalability, local dispersion relation can be expressed through the dispersion relation at the input:

$$k(\omega_0, z) = \frac{1}{\alpha(z)} k_0\big(\omega_0\,\alpha(z)\big) \tag{5.5}$$

where k_0 is the dispersion function at the input. We will also take into account the possible shift of the entire band diagram in frequency $\Delta\omega_{shift}(z)$ due to some change of parameters different from uniaxial deformation. Though no change of parameters will lead to an ideal shift of the dispersion relation without a change of its shape, in case of small parameter changes that can be a good approximation. Basically, we should look at the band diagram at the input and at the point of maximum change, and check how good it can be approximated by a simple shift. Thus, the wave vector dependency can be changed to:

$$k(\omega_0, z) = \frac{1}{\alpha(z)} k_0\big(\omega_0\,\alpha(z) - \Delta\omega_{shift}(z)\big) \tag{5.6}$$

Now we substitute this relation into (5.1):

$$\varphi(\omega_0, z) = \int_0^z \frac{1}{\alpha(z)} k_0\big(\omega_0\,\alpha(z) - \Delta\omega_{shift}(z)\big)dz \tag{5.7}$$

The time delay can be calculated as a first derivative of the phase response:

$$\tau(z) = \frac{\partial\varphi}{\partial\omega_0} = \int_0^z k_0'(\omega(z))dz \tag{5.8}$$

$$\omega(z) = \omega_0\,\alpha(z) - \Delta\omega_{shift}(z) \tag{5.9}$$

The new frequency $\omega(z)$ describes the shift of the band diagram, where the mode frequency ω_0 stays the same. The dependency of the integral argument is completely concentrated in the argument of the wavevector derivative, which corresponds to the local inverse group velocity. Thus, it is sufficient to know the band diagram at the input to calculate the time delay. In case of a monotonous dependency of $\omega(z)$ on z coordinate, which is generally the case, we can change the integration parameters:

$$\tau(z) = \int_{\omega_0}^{\omega(z)} \left(\frac{dk_0(\omega)}{d\omega}\right)\left(\frac{dz}{d\omega}\right)d\omega \tag{5.10}$$

We will consider a particular case of a linear chirp:

$$\alpha(z) = \frac{a_0 + z\Delta a / L}{a_0} \tag{5.11}$$

$$\Delta\omega(z) = \Delta\omega\frac{z}{L} \tag{5.12}$$

$$\omega(z) = \omega_0 + \frac{\Delta\omega_{chirp}}{L}z \tag{5.13}$$

where L is the length of the chirped structure and $\Delta\omega_{chirp} = (\Delta a / a_0)\omega_0 - \Delta\omega$. Thus, the derivative $d\omega/dz$ is a constant and simple integration is possible:

$$\tau(z) = L\frac{(k_0(\omega) - k_0(\omega_0))}{\Delta\omega_{chirp}} \tag{5.14}$$

The lattice constant change and the frequency shift are summarized together in the parameter $\Delta\omega_{chirp}$, which defines the maximum frequency shift of the band diagram, it is also the maximum operational bandwidth of the chirped structure. From (5.14) it is possible to see that the time delay is basically proportional to the wavevector change. Taking into account, that ω is also linearly proportional to the coordinate change (5.13), it is possible to show that the time function $t(z)$ is just a linearly scaled dispersion relation with factor $L/\Delta\omega_{chirp}$. Thus, the pulse propagation as a function of time has the same curve as the dispersion relation at the input and any maximum or minimum corresponds to the turning point. In Fig. 5.2a we show an example of a band diagram where $\alpha(z) \equiv 1$ and $\Delta\omega < 0$. The band diagram is gradually shifted down with the position in the grating. The group velocity decreases until the turning point is reached for the frequency ω_0. Afterwards the group velocity becomes negative, the band diagram moves up again and light goes out of the structure. We can also consider the band diagram at the input and scan it with the frequency ω (5.9), as it is shown in Fig. 5.2b.
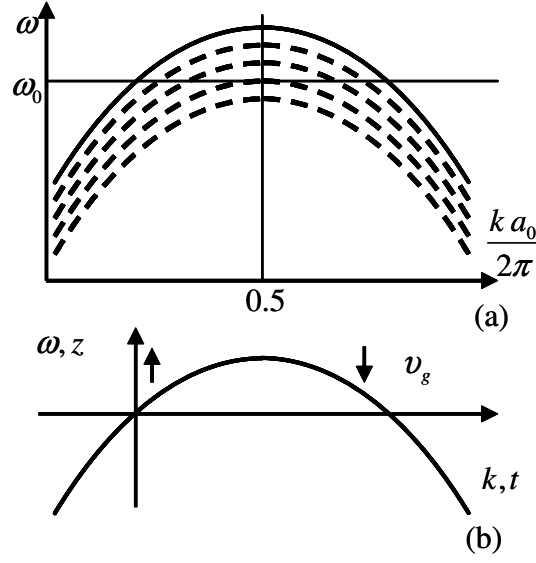
Fig. 5.2: The schematic band diagram shift and light propagation in a chirped periodical structure. (a) Band diagram is gradually shifted at different positions in the structure as shown with dashed lines. Light does not propagate in the part where there is no states. (b) Group velocity changes the sign at the turning point. Pulse propagation as a function of time is just the scaled dispersion curve.

Now we can derive the time delay as a function of the frequency ω_0. The light is traveling from input to the output, thus the full time delay is:

$$\tau = L \frac{\left(k_{output}(\omega_0) - k_{input}(\omega_0) \right)}{\Delta \omega_{chirp}} \tag{5.15}$$

where k_{input} and k_{output} are wavenumbers at input and output of the chirped structure correspondingly. The mostly used property of the chirped periodical structures is the second order dispersion. We can directly use the derivative of (5.15):

$$\frac{d\tau}{d\omega_0} = \frac{L}{\Delta \omega_{chirp}} \left(\frac{\alpha(L)}{v_{ouput}} - \frac{1}{v_{input}} \right) \tag{5.16}$$

where v is the group velocity. The dispersion can be directly obtained as:

$$D = \frac{d\tau}{d\lambda} = \frac{\omega_0}{2\pi c} \cdot L \cdot \left(\frac{\alpha(L)}{v_{ouput}} - \frac{1}{v_{input}} \right) \cdot \frac{\omega_0}{\Delta \omega_{chirp}} \tag{5.17}$$

Thus, dispersion depends on the group velocity difference at the input and output and the relative frequency shift of the band diagram.

5.3 Example of a high index contrast Bragg mirror

A high index contrast Bragg mirror is a problem were the conventional coupled mode theory fails to give correct results. In this section we will demonstrate our model on a quarter wave stack silicon/air with the index contrast 3.5 to 1. The relative chirp of the structure is achieved by the geometrical scaling

$$\frac{\Delta a}{a_0} = \frac{\Delta \omega_{chirp}}{\omega_0} = 1\% \tag{5.18}$$

The band with maximum is excited similar to shown on Fig. 5.2a. We start with the TMM calculation of a chirped Bragg stack 250 periodical units long excited from the air. The phase response of the structure is directly obtained from the reflection coefficient. The time delay is found as the first derivative over frequency. The time delay shows strong oscillations (Fig. 5.3a) due to the reflection at the input. This can be avoided by a special apodized coupling section [59]. We have also excited the structure with the Bloch mode directly. The reflection was calculated as the Bloch wave too, which is quite simple to calculate in transfer matrix formalism (see section 2.2). The conventional incident and reflected plane waves can be considered as a sum of incident and reflected Bloch waves:

$$q \cdot \begin{pmatrix} 1 \\ r \end{pmatrix} = 1 \cdot \begin{pmatrix} f \\ b \end{pmatrix} + r_B \begin{pmatrix} b* \\ f* \end{pmatrix} \tag{5.19}$$

where q is a constant and r and r_B are the plane wave and Bloch wave reflection coefficients correspondingly. When the reflection coefficient r of the plane wave is known, the reflection coefficient of the Bloch wave can be easily derived:

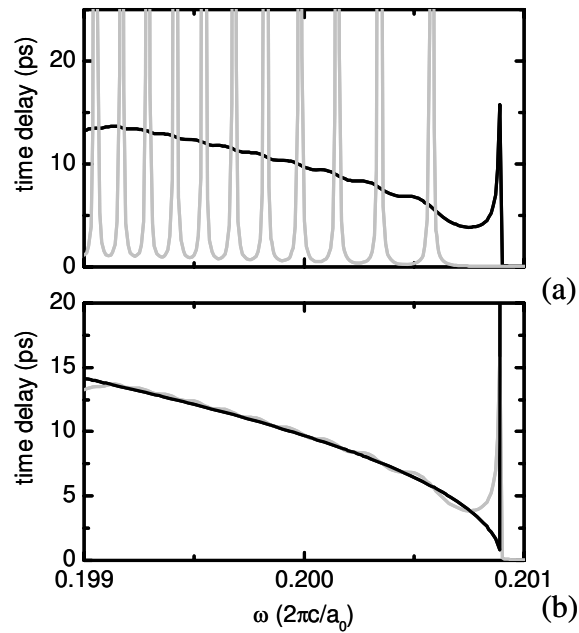$$r_B = \frac{b - ra}{rb* - a*} \tag{5.20}$$

Fig. 5.3: Time delay response of a linearly chirped quarter wave stack 250 lattice parameters long with the 1% lattice constant chirp. (a) The grey line corresponds to the direct excitation from air and the black line corresponds to the excitation with a Bloch mode. (b) The black line is the band diagram prediction of the time delay, the grey line is the time delay response simulated with the Bloch wave excitation.
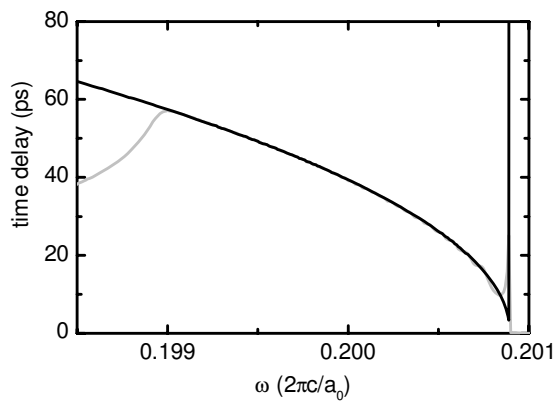

Fig. 5.4: Time delay response of a linearly chirped quarter wave stack 1000 lattice parameters long with the 1% lattice constant chirp. The black line corresponds to the band diagram prediction of the time delay and the grey line is the time delay response simulated with Bloch wave excitation. The band diagram gives a very good approximation of the time delay.

Reflection of the same stack excited with a Bloch wave is shown with a black line in Fig. 5.3a. The oscillations of time delay are strongly reduced, though still present, especially near the cut off frequency. Our approximation does not explain the residual slight oscillation. When Bloch mode excitation is used, no ripple would be expected. But this discrepancy is directly connected to the limitation of the adiabatic theorem. Basically, the ripples appear when the adiabatic theorem is not fulfilled and there is some coupling to the backward propagating Bloch mode. This is confirmed by the fact that the amplitude of oscillations decreases when a longer structure is calculated (Fig. 5.4). This can be explained by the reduction of the Bloch mode mismatch in the chirped structure, which is proportional to $\Delta\omega_{chirp}/L$. The residual reflection can be also explained as the first derivative mismatch at the input discussed in [59]. Time delay approximation of the long structure, 1000a, almost exactly corresponds to the TMM calculations (Fig. 5.4).

5.4   Example of chirped coupled line-defect waveguides

In this section we will investigate the structure proposed in [28], which consist of two coupled PC line defect waveguides. Coupled PC waveguides have already been discussed as directional couplers [61][64] and dispersion compensators (see chapter 4). The dispersion relations of the symmetrical and anti-symmetrical supermodes change dramatically with the number of rows that separate two waveguides [62][63]. There is also a possibility of decoupling, in this case symmetric and anti-symmetric modes have the same wavevector and frequency [64][62]. In [28] two waveguides were considered in a triangular lattice of holes (hole radii $r = 0.3a$ and refraction index $n = 2.963$). They have original bands with opposite slopes and the same band edge frequency (Fig. 5.5). One of the waveguides has W0.85 width ($W = \sqrt{3}\,a$) and the other has the same width but contains an additional row of holes ($r = 0.2525a$) in the middle section (see the inset of Fig. 5.5). To match the band edges of the two modes the precision of the holes radii in the additional row should be below one nanometer, otherwise the trimming procedure is needed after the manufacturing. By the chirp of the structure the modes are shifted gradually along the waveguides. At the point where frequency of the wave corresponds to the band edge frequency the light in the first waveguide is supposed to localize and couple to the second waveguide. The pulse propagation and time delay was calculated in Ref. [28].with a direct FDTD simulation.
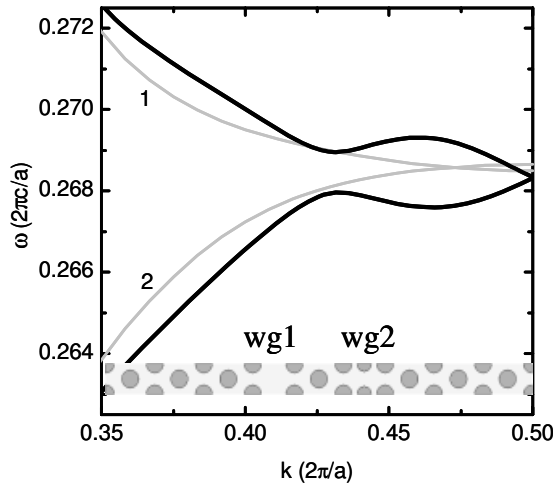
Fig. 5.5: The newly calculated band diagram of the coupled waveguide system from [28]. The black line is the dispersion relation of the coupled waveguides and the grey lines correspond to the dispersion relations of the single waveguides. The interaction of the waveguides leads to a dramatic change of the dispersion relation.

We would like to explain the complicated pulse propagation observed in the FDTD simulation and present a general equation for the time delay. First we calculated the band diagram of the coupled waveguides (Fig. 5.5). There are two points of weak coupling between two waveguides along the wave number axis. One at the normalized wave number approximately 0.43 and the other directly at the Brillouin zone edge. More important for our discussion is the decoupling at the band edge, that was already observed, for example in [61]. This decoupling occurs due to the π phase shift between the two standing waves in waveguides 1 and 2. The sum of these two standing waves can be considered as a propagating mode, thus the group velocity doesn't decrease to zero near the Brillouin zone edge. If we now unfold the band diagram, the dispersion relation goes smoothly through the Brillouin zone edge with finite slope. This is true only for the case of exact matching of the band edges, otherwise there is a small band gap.
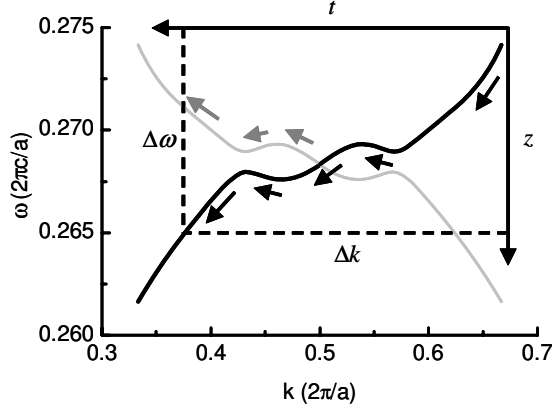
Fig. 5.6: The unfolded band diagram of coupled waveguides and pulse propagation in the chirped structure are shown with the black line. Black arrows show the time evolution of the transmitted signal and grey arrows follow the reflected signal. The pulse changes the direction of propagation four times.

We show the unfolded band diagram in Fig. 5.6. The chirp in [28] was achieved assuming an index change from 2.963 to 2.850 on the length of the structure. We use an approximation that the band diagram in this case only shifts in frequency by $\Delta\omega \approx 0.01 \cdot (2\pi c / a)$ without changing its shape, which means that $\alpha(z) \equiv 1$ in (5.6). As it was already discussed the function $z(t)$ is a scaled band diagram with a scaling factor $L / \Delta\omega$. Thus light propagating through such coupled waveguides structure has four turning points due to the sign reversal of the group velocity. The delay is therefore achieved not due to the light localization but due to the multiple back and forward propagation. This shouldn't be confused with the multiple reflections in the Fabry-Perot resonator. In the discussed structure at every turning point as group velocity reverses its sign perfect reflection takes place. This description exactly corresponds to the simulated pulse propagation shown in [28]. Some reflection back to the input can also be observed when the modes of two waveguides are not exactly matched at the Brillouin zone edge and the light will have to tunnel through a small potential barrier. The reflected light follows the path shown with a grey line in Fig. 5.6.

The time delay of this structure is proportional to the wavevector shift $\Delta k \approx 0.3 \cdot (2\pi / a)$ corresponding to the frequency chirp $\Delta\omega$:

$$\tau = L \frac{\Delta k}{\Delta\omega} \approx 30 \frac{L}{c} \tag{5.21}$$

Thus the average group index is 30. If $L = 100 \mu m$ is taken, we obtain a time delay $\tau = 10 ps$ which exactly matches the pulse propagation time obtained from FDTD simulation in [28]. Thus the exact shape of the modes near the band edge is not important, though initial modes should be flat to provide a large wavevector shift corresponding to a small frequency shift. The accumulated second order dispersion

depends on the difference of inverse group velocities at the input and output (5.17). It is favorable to have the same group velocities at the input and output, which makes the dispersion vanish. Such structures provide time delay of the signal without distortion and can be used for tunable time delay lines by chirp variation.

5.5   Dispersion compensation with chirped slow light waveguides

The chirped periodical structures are conventionally used for dispersion compensation [52][58]. In this chapter we will limit the discussion to the structures operating in reflection, where input coincides with output, to have direct comparison to chirped FBGs and Bragg mirrors. The light is traveling to the turning point and back, thus the full time delay from (5.15) is:

$$\tau = 2L \frac{\left(\dfrac{\pi}{a_0} - k_0(\omega_0) \right)}{\Delta\omega_{chirp}} \tag{5.22}$$

Thus, dispersion depends only on the group velocity at the input:

$$D = \frac{d\tau}{d\lambda} = \frac{\omega_0}{2\pi c} \cdot \frac{2L}{v_g} \cdot \frac{\omega_0}{\Delta\omega_{chirp}} \tag{5.23}$$

At the input always the mode with positive group velocity is excited, and the sign of dispersion is defined only by the sign of the frequency shift. For example in Fig. 5.2a the band diagram moves down and the $\Delta\omega$ is negative. Thus from (5.14) $\Delta\omega_{chirp}$ is positive and dispersion is positive. It means that by operating with a mode that has a maximum we get positive dispersion and operating with a mode that has a minimum we get negative dispersion.

Dispersion can be increased near the band edge of a one-dimensional structure, where group velocity is small. A certain bandwidth of constant dispersion is needed for the application, unfortunately the inverse group velocity near the band edge is highly nonlinear (see chapter 3):

$$\frac{1}{v_g} \sim \frac{1}{(\omega_{band\,edge} - \omega)^{1/2}} \tag{5.24}$$

As you can see from Fig. 5.4 the slope of the time delay becomes very steep near the band edge, but second derivative is not zero also, that leads to high third order dispersion. The second derivative decreases away from the band edge but slope also becomes flatter.

We will use the property of the PC line-defect waveguide to guide a mode with quasi constant small group velocity (see chapter 3). We will consider a 2D system so as to reduce the simulation volume und thus calculate longer chirped structures. The

results can be easily extended to 2D slab structures, the modes will still lie below the light line. The wavevector and the effective index of the guided mode in such PC waveguide are presented in Fig. 5.7. There is a bandwidth of about 0.5% of relative frequency where the group velocity is constant and 50 times slower as in air. Thus, we expect constant dispersion in the linearly chirped structure on this bandwidth. To demonstrate the uniqueness of the PC line-defect waveguide we show the wavevector and the effective index of a quarter wave stack with contrast of silicon to air. Though it has quite a flat band near the band edge compared to the structures with low index contrast [69], its effective index is still much smaller and highly nonlinear compared to PC line defect waveguide. The bandwidth of the group index 50 in the one dimensional structure will be far too small to be useful.
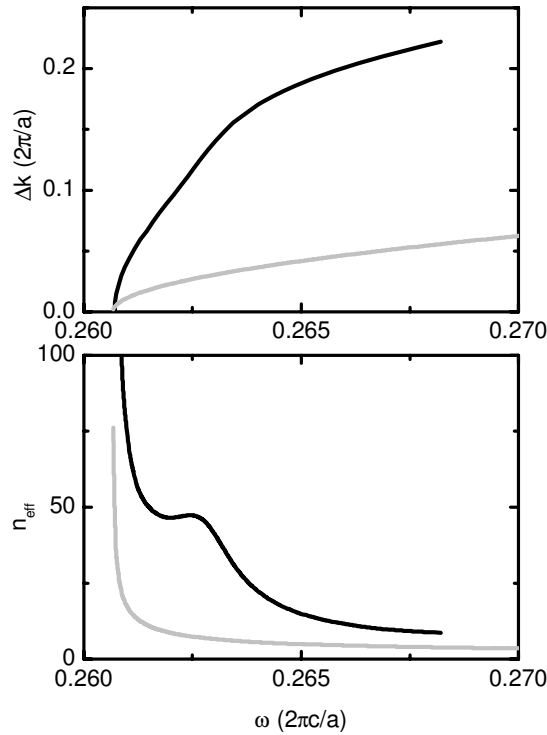

Fig. 5.7: (a) Band diagrams of a small group velocity PC line-defect waveguide (black line) and a quarter wave stack (grey line). Both have refractive index contrast of silicon to air (3.5 to 1). PC waveguide is formed in a triangular lattice of holes with radii r = 0.3a and waveguide width 0.7W. The band diagrams are normalized to the lattice parameter of the PC waveguide. The lattice parameter of the quarter wave stack is chosen to match the band edges of two structures. (b) Effective indices calculated as speed of light divided by the group velocity. The PC waveguide mode has a bandwidth of constant small group velocity.

We simulated the proposed structure using FIT software, Microwave Studio, CST. The lattice parameter was chosen to be 0.4μm, thus the operational frequency is close to 200 THz. The chirped section of the PC waveguide was 200 lattice constants long. The line-defect waveguide was created in a triangular lattice of holes with radii $r = 0.3a$. The waveguide was chirped by the width change from 0.71W to 0.69W ($W = \sqrt{3}\,a$) which corresponds approximately to a linear shift of the band diagram $\Delta\omega = 3.2\,\text{THz}$. The small shifts of the adjacent holes along the waveguide can not be resolved with the mesh lines of the finite integration method, but the average dielectric constant of the mesh cells changes and that produces the required chirp. It is difficult to provide Bloch mode excitation in the time domain simulations. We assumed normal butt-coupling from dielectric waveguide into PC waveguide. Strong time delay oscillations are observed, though the average delay follows the dependency predicted by the band diagram (see Fig. 5.8). If time delay ripples are suppressed there is a bandwidth of constant negative dispersion equal to 1 ps/nm. A hundred times longer structure with narrower bandwidth of 100GHz accompanied by further group velocity reduction can allow the 2000 ps/nm dispersion within 1cm length.
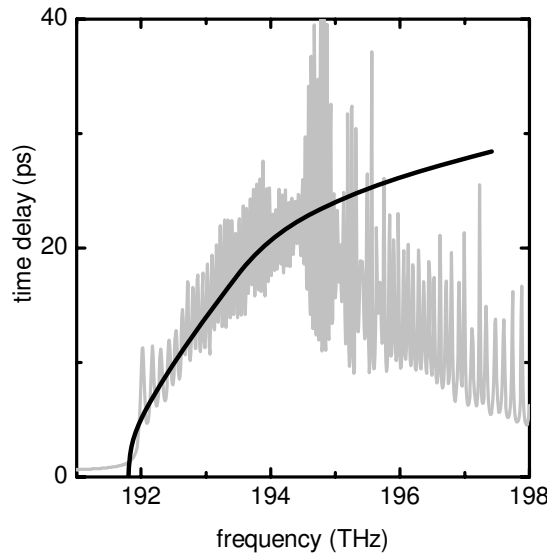

Fig. 5.8: Time delay response of linearly chirped PC line defect waveguide of 200 lattice constants long with chirp parameter $\Delta\omega$ of approximately 3.2 THz. The black line corresponds to the time delay predicted by the approximation and grey line is the time delay from the finite integration simulation. The oscillations on the time delay appear due to the reflections at the input.

Several measures can be taken to decrease the reflections. The adiabatic coupling can be used to couple from the index guided mode into the slow group velocity mode as described in chapter 6. Though in any case it is difficult to expect reflections

smaller than in apodized FBGs. Another more favorable solution would be a PC structure where input and output channels are separated, thus the reflected signal will not interfere directly with outgoing signal. PC waveguides are much more flexible in this case as FBGs.

5.6 Conclusion

We have developed a novel and efficient approximation to predict time delay and dispersion of linearly chirped PC structures. Based on the assumption of linear scaling and shift of the band diagram along the chirped structure we have managed to obtain a simple dependency between the band diagram and the pulse propagation. It was shown that time delay and dispersion depend on the wave vectors and group velocities differences at the input and output of the chirped structure correspondingly. Thus, to obtain a bandwidth of constant time delay we need to use waveguides with a constant wavevector difference at the input and output. To obtain a bandwidth of constant dispersion we need waveguides with constant difference of group velocities at the input and output. These considerations show the problem of the high index contrast Bragg stack application to dispersion compensation. Though there is a large group velocity difference at the input and output, this difference changes strongly with frequency and large third order dispersion is accumulated, that will distort the signal.

The presented approach can be applied to rather complex structures as for example coupled waveguide systems. It allows time delay predictions already from the band diagram obtained with much smaller computational effort as the exact calculation of the chirped structure. We also described the pulse propagation and explained some nontrivial phenomena as multiple pulse reflection within the chirped structure.

Based on the band diagram of a small group velocity PC waveguide we proposed a chirped structure with exceptionally large dispersion. Negative dispersion of 2000 ps/nm required for compensation of chromatic dispersion of the 100 km fiber can be obtained in a 1cm linearly chirped PC waveguide. It is approximately 10 times shorter than the chirped fiber Bragg grating with comparable dispersion due to group velocity reduction. Additional advantage can be obtained if the input and output channels could be separated. This could possibly be achieved with coupled PC waveguides.

6. Coupling to slow light waveguides

An efficient approach is presented to couple light into a slow light mode of a photonic crystal line-defect waveguide. The two stage coupling is proposed where a dielectric waveguide mode is first coupled into an index guided mode of a line-defect waveguide and the index guided mode is butt coupled or gradually changed into the slow light mode. The first stage can be optimized with adjustment of the boundary cut to have less than -35dB reflection. And the second stage with butt coupling to group velocity 0.02c demonstrates only -20 dB reflection. The second stage can be more efficient with adiabatic change of the structure. Coupling is demonstrated to slow light mode with group velocity 0.007c on 20 lattice constant long adiabatic coupling with overall reflection losses less than -32 dB. A comparison with one dimensional structure at the band edge is provided which shows the advantage of line defect modes.

6.1   Introduction

An important issue of slow light applications is the efficient coupling from dielectric waveguides [10][72][73][74]. We would separate two possible situations: coupling to "index guided" modes with group velocity and mode profile similar to the strip waveguide mode and coupling to slow light "gap guided" modes where the Bloch mode is very different from the strip waveguide mode. The adiabatic, gradual change of the structure is proven to be possible in any case [51][75]. But much shorter couplers were designed for index guided modes by adjustment of transparent resonance condition at the boundary [76][77] similar to anti-reflection coating applied in conventional optics. The bandwidth of such resonances is quite broad to be applied for WDM signals. This approach was also investigated for slow light modes [72]. Though the increase of transmission was registered for certain terminations of the photonic crystal interface, the measured transmission is still below -5dB and reflections approach 50% of the intensity. We propose to use the resonant approach for coupling light into PC line-defect waveguides and then transfer the "index guided" mode into slow light mode. The light

in this case can not be scattered from the junction as in the case of the coupling from dielectric waveguide and only reflection or coupling to other guided modes is possible. The adiabatic change of the structure will be investigated for the second junction similar to the discussed in Ref. [10].

Line-defect modes are considered in triangular lattice photonic crystal structures [6][25]. Normally the guidance in vertical direction is achieved due to the total internal reflection. We will consider only 2D models and disregard the third dimension in this chapter. The coupling losses occur mainly due to the mismatch in the 2D plane of the PC waveguide and thus the results obtained for 2D structures can be generally applied to the 3D slab PC structures. Though some additional vertical loss can be produced at the coupling interface, this loss is considered to be negligible in comparison to the one caused by the 2D mode mismatch. We are going to simulate structures with small reflections thus the boundary conditions of the simulation approach are becoming very important. We decided to use the Eigenmode Expansion Method implemented in the modeling tool CAMFR (see section 2.3). The 1D structure near the band edge are also calculated for comparison reasons. They are simulated with Transfer Matrix Method (see section 2.2).

The butt coupling approach to coupling at first and second stages will be discussed in section 6.2. Section 6.3 presents the adiabatic coupling model and simulation results. The results are summarized in section 6.4.

6.2   Butt coupling

The coupling to small group velocity $v_g = 0.02c$ in W0.7 waveguide presented in chapter 2 will be considered through a stage of W0.8 waveguide with group velocity $v_g = 0.25c$. In 2D calculations the radius was changed from $r = 0.275a$ in the chapter 2 to the $r = 0.3a$. Coupling to the slow light in W0.7 waveguide at wave number $k = 0.4$ will be considered (see Fig. 6.1). Thus the excitation frequency will be taken at approximately 0.263. The W0.8 mode is much steeper at this frequency as can be seen from the band diagram. The dielectric waveguide with the width equal to the line-defect waveguide will be considered and the cut to the photonic crystal will be varied with parameter $\tau = z / a$ (see Fig. 6.2), similar to the presented in Ref. [76].
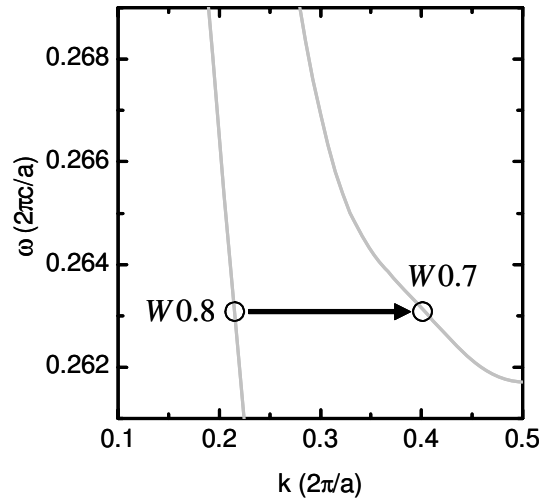
Fig. 6.1: The band diagrams of the W0.7 and W0.8 waveguides are presented. At the frequency 0.263, where W0.7 waveguide demonstrates small group velocity, the dispersion curve of the W0.8 waveguide is much steeper.
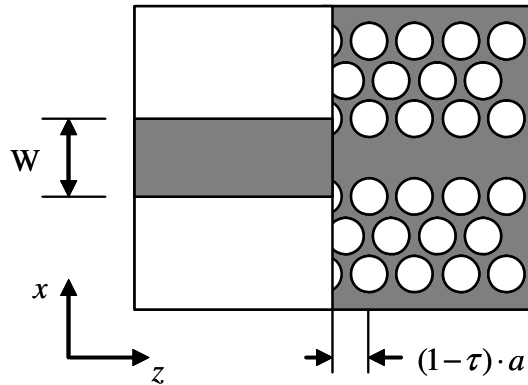

Fig. 6.2: The schematic picture of the junction between a dielectric waveguide and a PC line-defect waveguide. The boundary between two waveguides can be shifted in z direction, which is described by parameter τ.

The results for the direct coupling into W0.7 waveguide are presented in Fig. 6.3. Very strong reflection is observed for most of the boundary terminations. There are two points near $\tau = 0$ and $\tau = 0.2$ where reflection is small but at the same time transmission intensity is very low $T \approx 0.2$. Thus when reflection is small the scattering loss at the junction is increasing also. This can be explained by the fact, that slow light mode profile (see Fig. 2.1) is very different from the dielectric waveguide mode. The butt coupling into W0.8 waveguide is expected to be more efficient due to the better mode profile match.
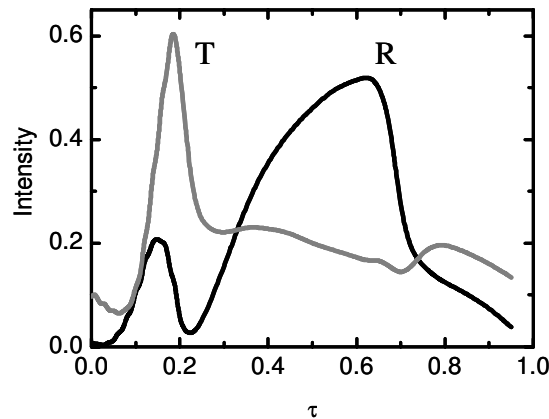
57

Fig. 6.3: The transmission T and reflection R intensities at the butt coupling to W0.7 waveguide from dielectric waveguide. Strong overall reflection is observed. At reflection minima the transmission is also low what corresponds to large scattering losses.
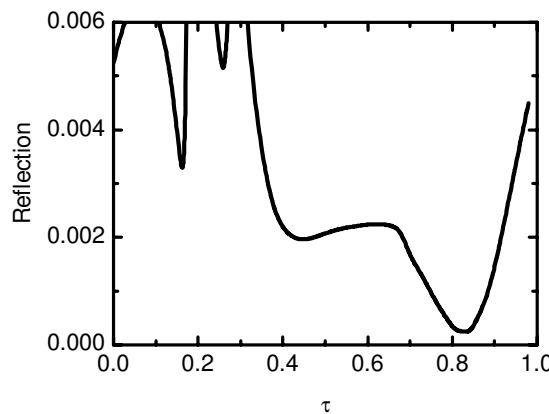
Fig. 6.4: The reflection intensity at the butt coupling to W0.8 waveguide from dielectric waveguide. Distinct reflection minimum is observed close to the boundary cut $\tau = 0.8$

The results of butt coupling to the W0.8 waveguide are presented in Fig. 6.4. Strong reflection reduction to -35dB is observed at $\tau = 0.82$. Transmission intensity is about 0.96 at this point. Thus almost perfect conversion from dielectric waveguide mode into photonic crystal mode is achieved. The light in W0.8 waveguide can be now transmitted into W0.7 waveguide with the butt coupling approach also. As shown in Fig. 6.5 the index guided mode is transformed into gap guided mode at the junction between two waveguides. the interface does not go directly through the holes. The holes on the line between two waveguides in Fig. 6.5 belong to W0.8 waveguide and the next

row of holes belongs already to W0.7 waveguide. The advantage of coupling from a line-defect waveguide is the absence of scattering losses due to the photonic band gap effect. Thus at the W0.8-W0.7 boundary only reflection is possible. The calculation gives the reflection intensity less than -20dB and transmission of 95% which is a very good result for such a simple coupling. These values were obtained for a single frequency calculation. The frequency scan shows that, though the reflection slightly increases close to the band edge of the W07 waveguide, it stays within -20dB on the 100GHz bandwidth. These coupling results are sufficient for the devices operating in transmission. But the reflection amplitude of 10% can still lead to strong ripple in the characteristics of reflection operating devices due to the Gires-Tournois interference. The second transition can be done adiabatically to decrease reflection to -40 dB as will be discussed in the next section.
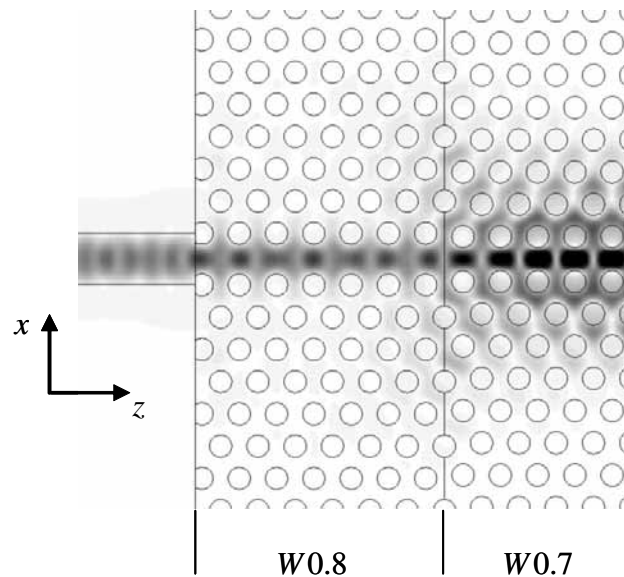

Fig. 6.5: The field distribution in the optimized double stage coupling. First light is coupled into W0.8 waveguide and then after 6 lattice constants it is coupled into W0.7 waveguide. The amplitude of the field in the W0.7 waveguide is large due to small group velocity.

6.3 Adiabatic coupling

6.3.1 Structures

The PC waveguide presented in Fig. 2.2 can be discretised with stair case approximation. For adiabatic coupling the model will be simplified to make possible a calculation of long structures. Square holes will be considered instead of cylindrical, thus decreasing the number of different cross sections in a single unit cell to two (Fig. 6.6). This simplification does not change significantly the properties of PC waveguide. Waveguide with square holes still demonstrates a bandwidth of constant small group

velocity discussed in chapter 3. By adjustment of the waveguide width to W0.8 the small group velocity of 0.007c is obtained on the 0.1% bandwidth. The group velocity is small in the gap guided mode region and increases at higher frequencies gradually changing to index guided mode. We will concentrate on coupling to the center frequency of slow light bandwidth $\omega = 0.2357$.
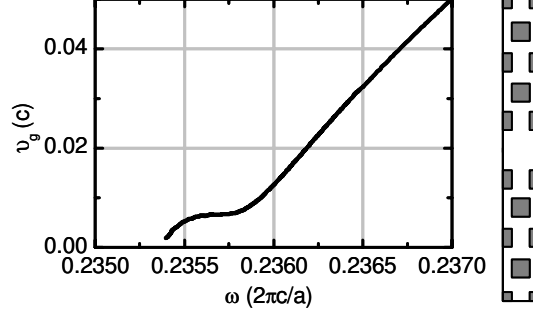

Fig. 6.6: The group velocity and the structure of a square hole triangular lattice PC line-defect waveguide ($r = 0.25a$, W0.8, $n = 3.5$, TE polarization). The holes are shown by grey color. There is a relative bandwidth of 0.1% with group velocity approximately $0.007c$.

A one dimensional Bragg stack also shows small group velocity near the band edge. We are going to consider this structure for comparison reasons. The one dimensional transfer matrix method (TMM) is applied to calculate the reflections. With parabolic approximation of the dispersion relation near the dielectric band edge we obtain that group velocity has the following frequency dependency (see chapter 3):

$$v_g = \frac{d\omega}{dk} \sim (\omega - \omega_0)^{1/2} \tag{6.1}$$

where ω_0 is the band edge frequency. This corresponds to the direct calculation of the group velocity near band edge for the quarter wave stack (Fig. 6.7). The bandwidth of small group velocity decreases quite rapidly. We choose the normalized frequency 0.2007 where group velocity is 0.035c. This group velocity is 5 times larger than the one calculated in the presented PC line-defect waveguide. The group velocity changes dramatically even on the relative bandwidth of 0.1%. Dispersion compensation is needed for the operation of such slow light mode as proposed in Ref [10].
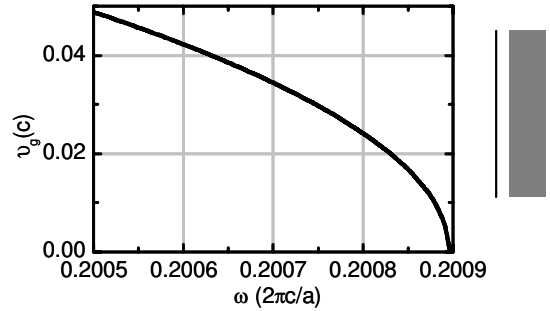
Fig. 6.7: The group velocity and the structure of a quarter wave stack of silicon and air (n = 3.5/1). The air gap is shown by the grey color. Group velocity 0.034c at frequency 0.2007 is calculated.

The input waveguide should have an index guided mode at the slow light frequency 0.2557. To keep the number of cross sections the same this waveguide is obtained with deformation along the propagation direction (Fig. 6.8a). The stretch factor is chosen to be 1.05. The band diagram of the deformed line-defect waveguide is quite similar to the original with the dispersion relation shifted to lower frequencies. The group velocity is approximately $0.13c$ at normalized frequency 0.2557. The same approach is used to couple slow light mode in a Bragg stack. A structure with smaller lattice constant has larger group velocity and can be resonantly coupled from homogeneous medium [77].

(a) (b)
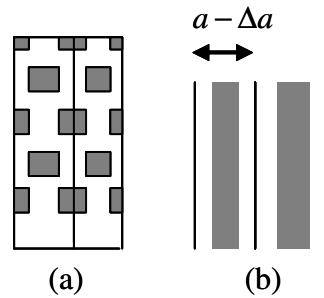
Fig. 6.8: The transitions between index guided and gap guided modes in a line defect waveguide and a Bragg stack. A symmetrical half of the line-defect waveguide is presented with the channel close to the bottom of the picture. The index guided mode propagates in the deformed waveguide on the left sides of figures (a) and (b).

Both discussed methods CAMFR and TMM allow boundary conditions of half-infinite periodical structure at the input and output. Thus it is possible to have Bloch mode excitation and to obtain transmission and reflection as Bloch modes too. This is done by presenting the Bloch modes in terms of slice eigenmodes and following

recalculation of the transmission and reflection matrices at input and output (see sections 2.2 and 2.3).

6.3.2   Theoretical model

The adiabatic coupling can be described by a simplified theoretical model. The adiabatic transition can be considered as a stepwise change from one ideal photonic crystal structure to the other. At every small step reflections occur that summate at the input with different accumulated phase shifts:

$$r = \sum_{n=1}^{N} \Delta r_n \exp\left(i \sum_{k=1}^{n} \Delta\beta_k \Delta z_k \right) \tag{6.2}$$

where r_n is the reflection at a step n, Δz_k is a distance between two steps and $\Delta\beta_k$ is a wavevector difference between forward and backward propagating modes. This is a first order approximation that doesn't take in to account second order reflection. It is applicable only for small reflection amplitudes. The sum can be also presented as an integral where gradual change of the photonic crystal structure is assumed [51]:

$$r = \int_0^L \frac{\partial r}{\partial z} \exp\left(\int_0^z i\,\Delta\beta(z')\,dz' \right) dz \tag{6.3}$$

In case of constant $\Delta\beta$ the integral is the Fourier transformation of a truncated function. If $\partial r / \partial z$ is also constant, then the larger the truncation region L the narrower the peak around zero in spatial frequency and thus the smaller the reflection value at the same $\Delta\beta$. This is a simplified prove of the adiabatic theorem. We can also rewrite the integral with the normalized length parameter $s = z / L$:

$$r = \int_0^1 f(s)\exp\left(i\,\Delta\beta\,L\,s\right)ds \tag{6.4}$$

where $f(s) = \partial r / \partial s$. In the case of constant reflection along the taper we obtain a sinc function in reciprocal space and thus with a longer taper the reflection amplitude decreases on average as $1/(\Delta\beta L)$. There are also some taper lengths when the sinc function and thus the reflection is zero, but this is a resonant phenomena and will have a narrow bandwidth. Better results can be achieved if the derivatives are matched at the input and output. Using the integration by parts, integral (6.4) can be presented as an infinite sum:

$$r = \frac{f(1)\exp(i\Delta\beta L) - f(0)}{i\,\Delta\beta\,L} + \frac{f'(1)\exp(i\Delta\beta L) - f'(0)}{(\Delta\beta L)^2} + \ldots \tag{6.5}$$

Thus every matched derivative of the order m leads to the asymptotic reflection decrease proportional to $1/(\Delta\beta L)^{m+1}$. In practice, the taper of final length with minimal reflection is needed. The required reflection function can be directly taken from the table of apodization (or window) functions that are used to suppress side lobes in the

Fourier spectra. The analytical approach is more complicated in case of not constant $\Delta\beta(z)$, the taper should be changed slower at the parts where $\Delta\beta$ is small. Alternatively an optimization calculation can be done similar to presented in Ref. [10].
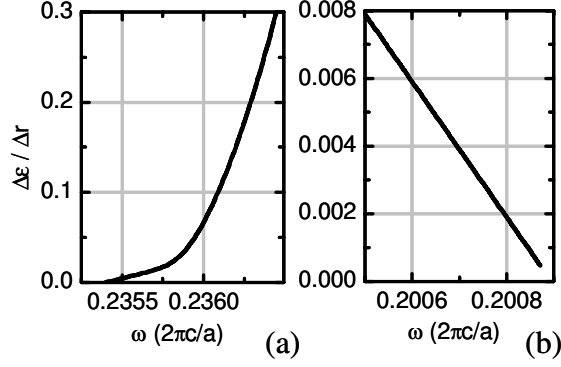

Fig. 6.9: The normalized inverse reflection on a deformation step is presented for a line-defect waveguide (a) and a Bragg stack (b). The Bragg stack demonstrates stronger reflection at the band edge with exactly inverse dependency on the frequency.

6.3.3   Reflection at the structural step

The reflection at a structural step is strongly frequency dependent. This dependency is determined by the group velocity and wavevector difference between forward and backward propagating modes as discussed in Ref [51]:

$$\Delta r \sim \frac{1}{\Delta\beta(\omega)v_g(\omega)} \tag{6.6}$$

This can be demonstrated by the direct calculations of a Bragg stack and a PC line-defect waveguide reflection at deformation step of $\Delta\varepsilon = \Delta a / a = 10^{-5}$. The reflection is proportional to $\Delta\varepsilon$ and a normalized reflection value is considered $\Delta r / \Delta\varepsilon$. In a one dimensional structure the wavevector difference is proportional to the square root of the frequency $\Delta\beta \sim (\omega-\omega_0)^{1/2}$ same as the group velocity (see (6.1)). Thus the inverse reflection is a linear function of frequency $1/\Delta r \sim (\omega-\omega_0)$ what corresponds to the dependency in Fig. 6.9b. The reflection values of 1D and 2D structures can be compared. The Bragg stack shows much stronger reflections at the same group velocities. Even without calculation of the adiabatic tapers we can state that slow light modes of PC line defect waveguides will be much easier to couple at the same group velocities. The reason for this result can be explained by the $\Delta\beta$ of these structures. The Fig. 6.10 shows the band diagrams of the line-defect waveguide and the Bragg stack near the band edge. First of all the slow light mode of the line-defect waveguide is further from the Brillouin zone edge than the Bragg stack mode, thus the $\Delta\beta$ has less influence on the reflection. The $\Delta\beta$ is calculated as $2(0.5-k)$ and for the slow light in line-defect waveguide it is approximately 0.15 and in the Bragg stack it is 0.02. This

makes up for almost an order of magnitude difference in reflection for the same group velocity (see eqn. (6.6)).
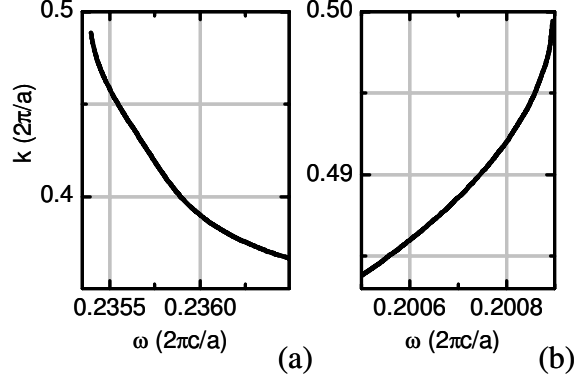

Fig. 6.10: The band diagrams of the line-defect waveguide (a) and the Bragg stack (b). The wavevector of the Bragg stack is much closer to the Brillouin zone edge as the line-defect waveguide.

6.3.4   Results and discussion

Different taper functions $\varepsilon(z) = \Delta a(z)/a_0$ can be investigated. The function $\partial r/\partial z$ from (6.3) can be written as a multiplication $(\Delta r/\Delta\varepsilon)\cdot(d\varepsilon/dz)$. The first part was calculated in the previous section. We will approximate the deformation of the lattice as a shift of the band diagram. The band diagram of the waveguide with deformation $\varepsilon_0 = 0.05$ is shifted by the relative normalized frequency $\Delta\omega/\omega \approx 0.02$ in comparison to the band diagram of $\varepsilon = 0$ waveguide. At the slow light part of the taper the normalized reflection $\Delta r/\Delta\varepsilon$ is very large and it should be compensated by smaller taper derivative $d\varepsilon/dz$ (see Fig. 6.11). We have considered a general form of the taper with parameter n

$$\varepsilon(z) = \varepsilon_0 \cdot \left(\frac{L-z}{L}\right)^n \tag{6.7}$$

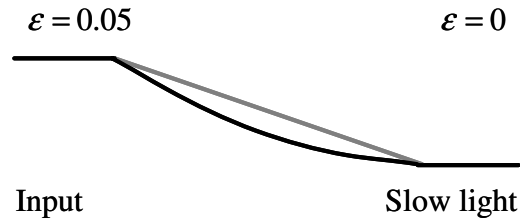$\varepsilon = 0.05$ $\varepsilon = 0$

Input   Slow light

Fig. 6.11: Examples of taper functions $\varepsilon(z)$ are presented. The grey line corresponds to linear taper. A slower taper at the slow light region should be applied as shown by the black line.

The reflection intensity in the line-defect waveguide for different tapers is presented in Fig. 6.12. Reflection at the transition without taper is less than 2%. The upper curve corresponds to the linear taper $n = 1$ and the curve under it corresponds to the quadratic taper $n = 2$. The black line corresponds to the $n = 3$ taper. The linear and quadratic tapers do not show any ripples on the reflection dependency. It means that the reflection at the input is much smaller than at the slow light output and there is no interference of two reflections. When the taper at the slow light region is sufficiently smooth than the two reflections become comparable and the Fabry Perot interference is observed as in the $n = 3, 4$ tapers. The difference between the $n = 3$ and $n = 4$ is not so large. To achieve better results we should then optimize the taper following the procedure described in Ref. [10], but we don't expect to achieve dramatic taper length reduction. The cubic taper shows reflection reduction up to -40dB at the length of the taper approximately $20a$.
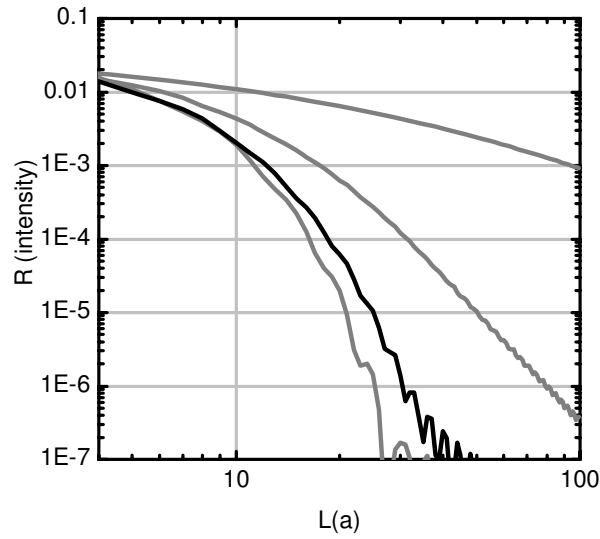
Fig. 6.12: Reflection intensity of the adiabatic taper in the line-defect waveguide as a function of taper length for the parameters $n = 1,2,3,4$ top down. The reflection is less than 2% without taper. It can be decreased to -40dB in a cubic taper $20a$ long.

The results for the Bragg stack adiabatic coupling are shown in Fig. 6.13 for comparison. At the input the structure is chosen with group velocity $v_g = 0.13c$ equal to the group velocity of the index guided mode of the line-defect waveguide. The slow light mode is to be excited at the normalized frequency $\omega = 0.2007$ with group velocity $v_g = 0.035c$. The lattice deformation in this case changes from $\varepsilon_0 = 0.0135$ to $\varepsilon = 0$. The tapers with $n = 1,2,3$ are calculated. The taper lengths should be an order of magnitude longer to achieve the same reflection suppression as with line-defect waveguides. Without taper more than 30% reflection is observed. The Fabry-Perot ripples are visible even for the linear taper. This is a sign for the strong reflection even at the input where group velocity is large.
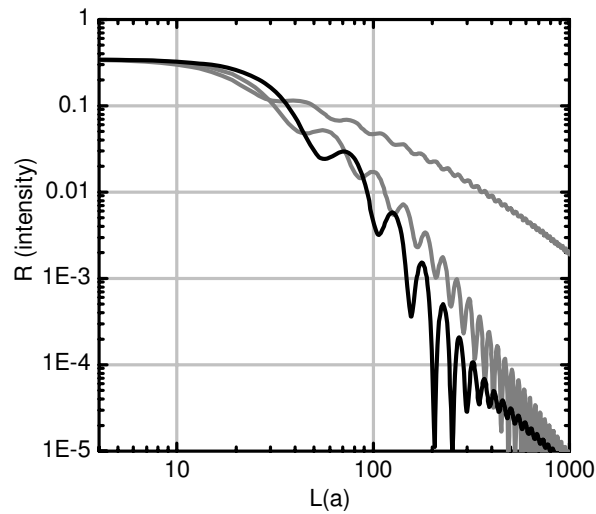
Fig. 6.13: Reflection intensity of the adiabatic taper in the Bragg stack as a function of taper length for the parameters $n = 1,2,3$ top down. The reflection is less than 2% without taper. It can be decreased to -40dB in a cubic taper $300a$ long.
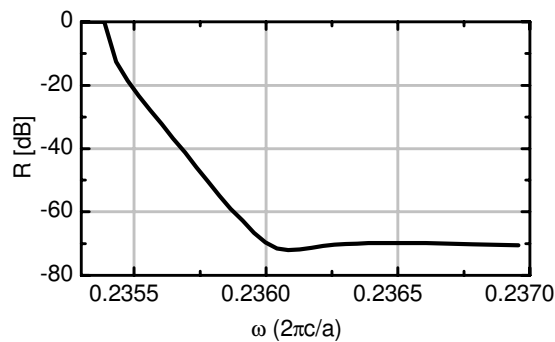
Fig. 6.14: Reflection intensity of the cubic taper $20a$ long. The reflection changes linearly from -32dB at $\omega = 0.2356$ to -52dB at $\omega = 0.2358$.

The adiabatic taper should allow coupling to a bandwidth of frequencies corresponding to the slow light mode. It extends from normalized frequency 0.2356 to 0.2358 as follows from Fig. 6.6. The relative bandwidth of this region is approximately 0.08% what corresponds to 170 GHz bandwidth for 1.5μm wavelength. The cubic taper of $20a$ long was calculated with result presented in Fig. 6.14. The reflection changes linearly from -32dB at $\omega = 0.2356$ to -52dB at $\omega = 0.2358$. The maximum reflection amplitude in this case is below 2.5%. This value can be decreased by using a longer taper.

6.4   Conclusion

The double stage coupling to the slow light waveguide has demonstrated very good transmission and reflection characteristics. The reflection at the first stage was reduce to -35dB by the proper adjustment of the W0.8 waveguide boundary termination $\tau = 0.82$. The second transition from W0.8 to W0.7 demonstrates reflection less than -20dB. The scattering loss in the second section is absent. Though in case of three dimensional structure some additional vertical scattering can occur, this scattering is expected to be small.

Adiabatic tapers can be used to decrease reflection at the transition to the slow light mode. The taper should change more slowly at the small group velocity region, thus different nonlinear functions are investigated. With 20 lattice constant long cubic taper the reflection of coupling from $0.13c$ group velocity to the $0.007c$ group velocity was decreased to the -32dB on the 170 GHz bandwidth. Further reflection reduction can be achieved with longer tapers and optimization of the taper function.

The slow light in the line-defect waveguides is much easier to couple to than in the one dimensional Bragg stack structure. The slow light in the 1D structure is achieved close to the Brillouin zone edge. Thus the difference in wave numbers of the forward and backward propagating modes is very small what leads to strong reflection.

7. Disorder induced backscattering

Disordered Bragg stacks and line-defect waveguides in two dimensional photonic crystal structures are considered. First, the reflection at a single defect is calculated and the results are used to estimate the reflected intensity in the disordered structure with statistical distribution of defects. The dependencies of the backscattering intensity on the group velocity and disorder amplitude are investigated. The backscattering puts strong limitations on the length of slow light waveguides.

7.1 Introduction

Small propagation loss is an essential condition for the application of slow light phenomenon. Disorder induced losses in the slow light waveguides are investigated experimentally [25][78] and theoretically [79][80][81]. They consist of two parts: vertical scattering and backscattering into the guided mode propagating in the opposite direction. The vertical scattering is considered to be dominant for the not slow light modes of line-defect waveguides. This loss was estimated by Gerace and Andreani [79][82]. And their results showed good agreement with experimental results of McNab et al. [25]. The loss was estimated to grow proportional to the inverse group velocity and thus dramatically increase for slow light modes. But the vertical scattering does not lead to the additional reflection and in-line amplification can be used to compensate for the losses. On the other hand, the backscattering loss is predicted to increase with inverse group velocity squared [83][80], what makes it a dominant loss factor at small group velocities [81]. At the same time, the backscattering can lead to strong coupling between forward and backward propagating modes in strongly disordered structures. This coupling results in localization effects similar to known in other disordered media [84]. This localization will destroy the phase information of the signal and thus will fundamentally limit the slow light application to optical communication systems. Thus, if the vertical loss intensity can be much larger than the output intensity of the device, the backscattering loss should be always significantly smaller than the output intensity.

Amplification will not help in this case, because both forward and backward propagating waves will be amplified. Taking into account the crucial effect of backscattering on the future applicability of slow light structures, we decided to concentrate on the backscattering calculation for the simplified one and two dimensional structures without consideration of vertical losses.

In section 7.2 we describe the simplified slow light structures. Section 7.3 presents the model to estimate the backscattered intensity. The disorder induced reflection in 1D and 2D structures are calculated in section 7.4. The results are discussed in section 7.5 and summarized in section 7.6.

7.2 Disordered slow light structures

The structures presented in section 6.3.1 are used for the simulations. The disorder is introduced in the structure by the random shifts of the boundaries. This corresponds to the manufacturing inaccuracies appearing due to the deviations of the electron beam from the prescribed lines. In the line-defect waveguide shifts of the longitudinal and lateral boundaries are considered as shown in Fig. 7.1a, defined as shift 1 and 2. In the one dimensional structure the boundaries between all layers are shifted.
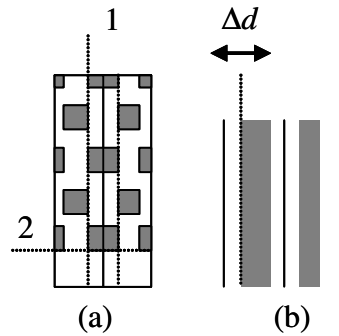
Fig. 7.1: The boundary shifts of the disordered 1D and 2D structures. (a) A symmetrical half of the line-defect waveguide is presented with the channel close to the bottom of the picture. In the line-defect waveguide the boundaries 1 and 2 were shifted. (b) In the quarter wave stack the boundaries between air and silicon were shifted.

7.3 Theoretical model

The small boundary variations in the periodical structures lead to Bloch modes scattering. If reflections are small then the second order reflections can be neglected. All scattered waves build a reflected wave at the input which can be mathematically described as a sum of reflections at every boundary with corresponding phase shift:

$$r = \sum_{n=1}^{N} \Delta r_n \exp(i\Delta\beta \cdot z_n) \tag{7.1}$$

where Δr_n is the reflection at the boundary n, z_n is a distance to the boundary from the input and $\Delta\beta$ is a wavevector difference between forward and backward propagating modes. N corresponds to the number of defects in the structure. For an arbitrary structure the reflection can vary, depending on the distribution of the defects. We will be interested in the mean value of the reflected intensity to estimate the effect of group velocity on the reflection intensity. The average reflection intensity can be calculated as:

$$\langle R \rangle = \langle r * \cdot r \rangle = \left\langle \sum_{n=1}^{N} \Delta r_n \exp(-i\Delta\beta \cdot z_n) \sum_{k=1}^{N} \Delta r_k \exp(i\Delta\beta \cdot z_k) \right\rangle \tag{7.2}$$

The sums in the brackets can be multiplied. The mean value of the reflection amplitude is zero $< \Delta r > = 0$. Thus, only multiplication terms from the same boundaries will remain:

$$\langle R \rangle = N < \Delta r^2 > \tag{7.3}$$

Thus average reflection intensity is just the sum of the average intensities reflected from every boundary. This corresponds to the summation of multiple incoherent sources. In this case, it is sufficient to find reflections from single defects to get an estimation of the reflected intensity. It should be mentioned that this estimation is valid only for the small reflection intensity when second order reflections can be neglected.

Another important parameter for slow light applications is the time delay ripple due to the disorder. The ripple can be explained as an effective interference of an output signal with the second order backscattered light. The simplest estimation would be a Fabry Perot interferometer with small reflections at the interfaces equal to $\langle R \rangle$. The average relative group delay ripple can be estimated in this case as:

$$\frac{\Delta\tau}{\tau} < 2\langle R \rangle \tag{7.4}$$

Thus to keep the delay ripple smaller than 1 percent a backscattered intensity should be smaller than half percent.

As discussed in papers [83][80][85] the reflection amplitude from a single defect is proportional to inverse group velocity $1/v_g$. Thus reflection becomes strongly frequency dependent. At the same time the reflection amplitude will be proportional to the boundary shift Δd presented in Fig. 7.1. Thus, generally we will define a normalized parameter $\Delta r(a/\Delta d)$. A dimensionless parameter α connects normalized reflection at the defect with the inverse normalized group velocity:

$$\Delta r\left(\frac{a}{\Delta d}\right) \approx \frac{\alpha}{v_g/c} \tag{7.5}$$

The larger α the stronger the reflection with the same boundary shift and the same group velocity. It effectively describes how strong the field is concentrated at the defect. When α is known, the reflections from the defects can be directly found from the boundary shifts and group velocity.

7.4   Results

7.4.1   Bragg stack

We start from the calculation of the average reflected intensity in the disordered 1D structure 500 lattice constants long. The reflection intensity was averaged on 100 structures for every frequency point in the range near the band edge. Afterwards the frequency dependency was presented as a group velocity dependency. The disorder was introduced with normal distribution of the boundary shifts with three different standard deviations of boundary shifts $\Delta d / a$: 0.001, 0.0005, 0.00025. These values are not determined by the manufacturing accuracies but are considered for demonstrational reasons. The reflection graphs are presented in Fig. 7.2 with largest reflection corresponding to the largest boundary shift. At small reflection intensity there is a clear $1/v_g^2$ dependency. This corresponds well to the theoretical predictions of [85]. The approximation is not valid for larger reflection intensity where strong coupling between forward and backward propagating waves takes place.

The calculated intensities can be estimated with the model developed in the previous section. The inverse normalized reflection amplitude from a single boundary shift $\Delta d / a / \Delta r$ is presented by a line in Fig. 7.3. This dependency is exactly proportional to the group velocity as can be seen by comparing to the Fig. 6.7. The parameter α of equation (7.5) is approximately 2.0. The average reflection amplitude was also recalculated from the disordered structures with the help of equation (7.3) and plotted as grey dots in the same figure. The number of defects in the structure was taken as 1000 taking into account two boundaries in one lattice constant. The estimation of the reflection amplitude fits to the direct calculation. Only at the band edge where the approximation is not valid any more there is some discrepancy between two graphs. These results allow the conclusion that any long disordered structure can be evaluated from the reflection behavior of a single defect.
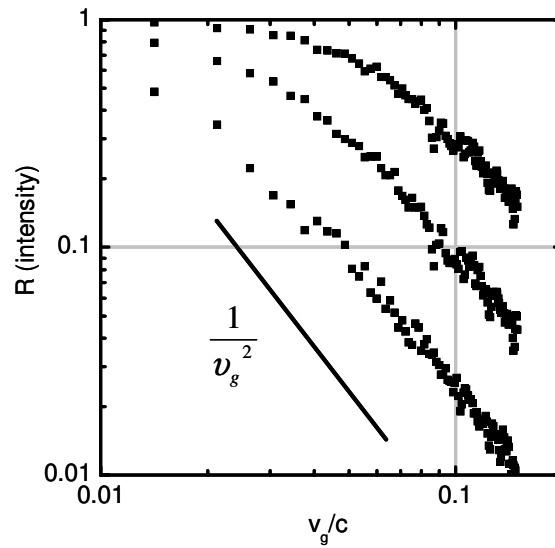
Fig. 7.2: The average reflection intensity of 100 disordered structures 500 lattice constants long as a function of group velocity. Three values of root mean square of the boundary shift are taken $\Delta d / a = 0.001, 0.0005, 0.00025$. The curve with the largest reflection corresponds to the largest disorder.
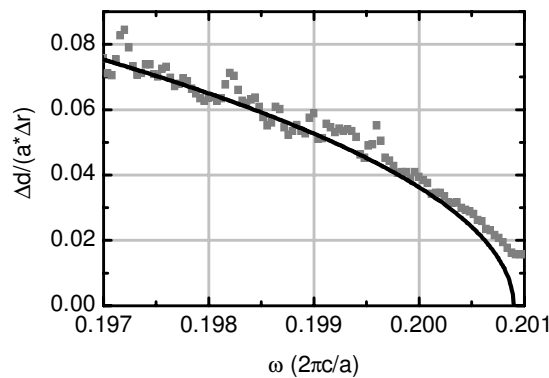
Fig. 7.3: A normalized inverse reflection amplitude at a single boundary shift of a quarter wave stack structure as a function of normalized frequency. The black line corresponds to direct calculation of a single defect. Points are calculated from the data in Fig. 7.2 and equation (7.3).

The next parameter to be investigated is the time delay ripple of the disordered structure. The relative time delay ripple of a single structure 500 lattice constant long with $\Delta d / a = 0.0005$ is presented with a thick black line in Fig. 7.4. The Fabry-Perot estimation of the time delay ripple given by equation (7.4) is presented by the thin black

lines. The estimated values are larger than the average calculated ripple. This can be explained by the distributed nature of the disorder induced reflection. The effective resonator length is thus smaller as the waveguide length and the phase and time delay oscillations have also a smaller value as estimated.
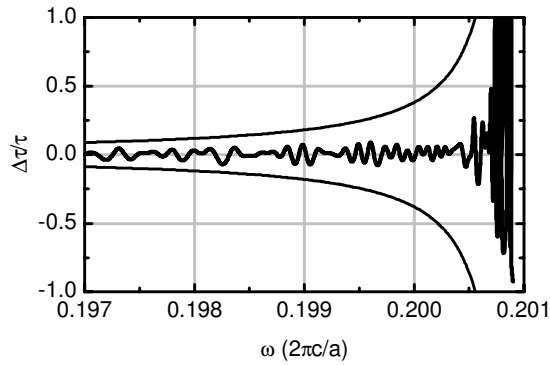

Fig. 7.4: Time delay ripple in the 1D disordered structure 500 lattice constants long with $\Delta d / a = 0.0005$. The estimation of the maximal time delay ripple given in the equation (7.4) is presented as a thin black line.

The reflection intensity near the band edge is demonstrated in Fig. 7.5. At frequency 0.200845 there is a transmission maxima with Q-factor approximately 200000. This resonance can be explained by the strong localization behavior at small group velocities. The localization length is decreasing at smaller group velocities, thus, at some point, it becomes smaller than the structure length and transmission can occur only through localized modes at certain resonant frequencies.
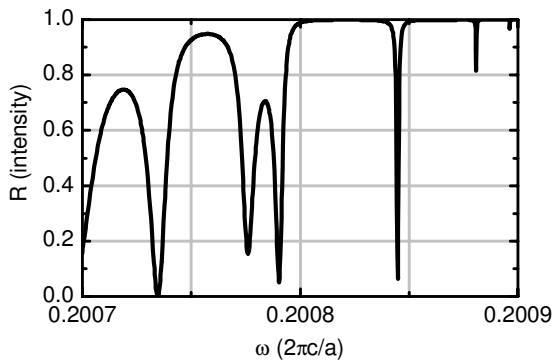

Fig. 7.5: Reflection intensity of a 1D disordered structure 500 lattice constants long with $\Delta d / a = 0.0005$. The dependency close to the band edge at very small group velocity is presented. Narrow minima are observed that correspond to transmission through localized modes.

7.4.2   Slow light line-defect waveguide

Reflection at boundary shifts 1 and 2 are considered in 2D waveguides as shown in Fig. 7.1. The normalized inverse reflections $\Delta d / a / \Delta r$ at these defects are presented in Fig. 7.6. The upper curve corresponds to the shift of boundary 1 and lower curve to the shift of boundary 2. The reflection has clear group velocity proportionality. The parameter α from equation (7.5) is equal to 0.23 for the boundary 1 and 0.84 for the boundary 2. As can be expected the shift of the boundary 2, which is the closest to the waveguide channel, is crucial for the backscattering. The reflection intensity in his case is more than 13 times larger than from the defect of the boundary 1.
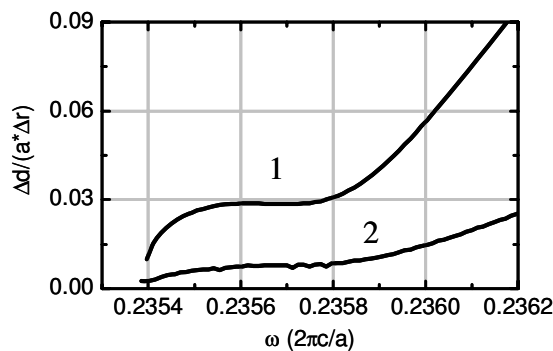

Fig. 7.6: A normalized inverse reflection amplitude at boundary shifts in 2D line-defect waveguide as a function of normalized frequency. The upper curve corresponds to the shift of boundary 1 and lower curve corresponds to the shift of boundary 2.

7.5   Discussion

The discussion section will be divided in three parts. We will compare 1D and 2D structures, discuss the effect of field concentration on the backscattering intensity and estimate the maximal length of the disordered structures.

7.5.1   2D versus 1D structures

The α parameters should be considered to compare 1D and 2D structures. We can see that the reflection at the boundary shift of the 1D structure is more than two times larger than the reflection at the shift 2 in the channel waveguide. This difference results in more than 4 times stronger reflection intensity in 1D structures at the same root mean square of the boundary shift and at the same group velocities. This can be explained by a smaller interaction with the defects in the channel waveguide. The large portion of the field is concentrated in the channel and doesn't interact with photonic crystal walls whereas in the one dimensional structure the shift of the boundary effects the entire field. Thus the 2D PC channel waveguide is generally less sensitive to disorder than the 1D structure. However, this two times difference of α is not very

large and thus slow light line-defect does not have strong advantage over 1D structure near the band edge.

7.5.2   Field concentration

As discussed in Ref. [85] the reflection from the defect is proportional to the amplitude of the field squared:

$$\Delta r \sim E^2 \tag{7.6}$$

Thus at small group velocities the amplitude of the field should be low at the places of possible disorder. This idea was already demonstrated in the calculations of Gerace and Andreani [86]. They shifted the waveguide walls outwards and thus decreased the amplitude of the field on the hole boundaries. However, this approach was applied only to index guided modes and it is difficult to follow for slow light modes, where strong interaction with the PC holes is intrinsic. But this consideration can be used to compare different slow light structures.

It is interesting to compare coupled cavities waveguides [18] with line-defect waveguides on the basis of equal group velocity and disorder. The field concentration arguments allows to draw a clear conclusion in favor of line-defect waveguides. Taking the power flow definition of the group velocity:

$$\upsilon_g = \frac{Power\ flow}{(W_E + W_M)/\Lambda}, \tag{7.7}$$

where power flow through waveguide cross section is taken, and W_E and W_M are the energies of the electric and magnetic field correspondingly in the unit cell of length Λ. Both types of waveguides are taken with the same power flows and group velocities. Thus the average energy per unit length should be equal for coupled cavity and line-defect waveguides. We will consider a coupled cavity waveguide with periodicity $\Lambda = ma$, where m is an integer. The field is mostly concentrated in the central section of length a within this period Λ. If the field energy is almost entirely concentrated in the center, then the intensity of the field is m times larger there than in the line defect waveguide. That leads to m times larger reflection amplitude at the defect due to the equation (7.6). Taking into account that coupled cavity waveguide has m times less scattering points, it follows from the equation (7.3):

$$\langle R \rangle_{CC} = \frac{N}{m} < (m \cdot \Delta r)^2 > = m \langle R \rangle_{LD}, \tag{7.8}$$

where $\langle R \rangle_{CC}$ and $\langle R \rangle_{LD}$ are reflection in disordered coupled cavity and line-defect waveguides correspondingly. Coupled cavities waveguides will have approximately m time stronger reflection for the same disorder. Thus, to decrease the reflection, the concentration of the field along the waveguide should be avoided.

7.5.3 Maximal length

The maximal length of the disordered structures is limited by the scattered reflection and maximal time delay ripple. We set a limit of the reflected intensity to $R_{max} = 0.1$. Combining equations (7.3) and (7.5) an equation can be obtained that connects maximal number of periods and group velocity:

$$N = R_{max} \left(\frac{a}{\Delta d} \right)^2 \frac{(v_g / c)^2}{\alpha^2} \qquad (7.9)$$

Thus the smaller is the group velocity the smaller is the maximal length of the structure. The parameter $\alpha = 0.84$ is taken for the boundary shift of the line-defect waveguide. We plot the length over group velocity for three shift parameters $\Delta d = 0.5, 1, 2\,\text{nm}$ in the Fig. 7.7. The lattice parameter was estimated by 500nm. From the figure it is possible to see that the normalized group velocity around 0.01 allows only very short structures. The reflection intensity of 10% is achieved already within several lattice constants.
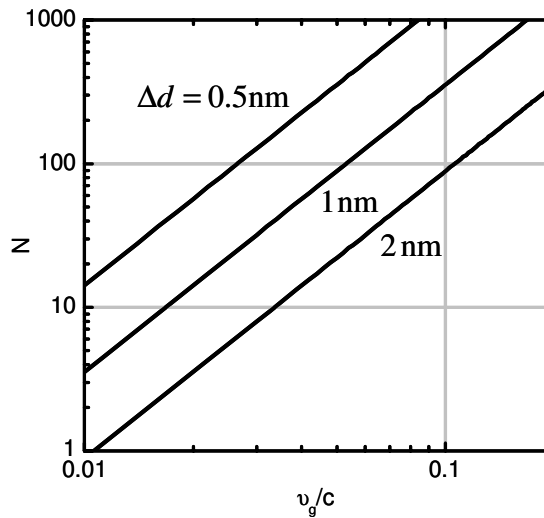
Fig. 7.7: The length of the disordered structure measured in lattice constants as a function of normalized group velocity. At these lengths the reflection intensity due to the back-scattering reaches 10%. The root mean square of boundary shifts are 2, 1, and 0.5 nm

These results can be compared to the vertical scattering estimated from the paper of Andreani et al. [82]. They varied the radius of the holes what is quite similar to the boundary shift in our investigation. For the radius deviation of 1nm the vertical scattering loss in the W0.7 waveguide with group velocity 0.02 is approximately 4dB/mm (approximately 60% scattering loss in $2000a$ structure). At the same disorder and group velocity, 10% reflection due to backscattering is achieved in the structure

shorter than 20 lattice constants. Thus the backscattering loss is a dominant scattering factor at small group velocities. It also corresponds to the results obtained by Kuramochi et al. [81].

7.6   Conclusion

The inverse proportionality of the reflection amplitude at the defect to the group velocity of the mode was confirmed. At the same group velocity the line-defect waveguide modes are less sensitive to the disorder than those in 1D quarter wave stacks. This is achieved due to the smaller amplitude of the field at the scattering defects. The further conclusion from this consideration is the advantage of the line-defect waveguide over coupled cavity waveguides. The field is distributed uniformly along the line-defect waveguide in contrast to strong field concentration at the cavity sites in the coupled cavity waveguides.

The length of the slow light waveguide is strongly limited by the backscattering. At maximal reflection intensity of 10% and 1nm shift of the hole boundaries the normalized group velocity should be larger than 0.05 to allow useful lengths of 100 lattice constants. These results make difficult the application of slow light to optical buffers. The time delay in this case cannot exceed several picoseconds, which is far to small to delay a packet of data. Though 100 lattice constants can be still sufficient for phase shift application in miniaturized Mach-Zender interferometers [17]. The current precision of photonic crystal manufacturing can be estimated from the work of Gerace and Andreani [79]. At radius of holes variation equal to 5nm the propagation loss is calculated to be approximately 2,7dB/mm for normal group velocity waveguide which correspond well to experimental results of McNab et al. [25]. The best reported propagation loss results at the moment are around 0.6dB/mm [26]. Taking into account that propagation loss scales with the square of the radius deviation, we can estimate the current radius variation to be approximately 2,5nm. The progress in the last two years was quite small, what can be attributed to the fact that 0,6dB/mm is already a sufficiently low loss for optical waveguides. But for slow light applications the precision should be further improved to allow long structures and large delays. At precision of 1 angstrom the structure can be already 400 lattice constants long with group velocity 0.01 speed of light. There are some other reasons to expect longer slow light structures. The calculations presented in this article are based on the 2D approximations. In real case some intensity will be lost vertically or absorbed. When these losses are larger than backscattering, then the localization effects can be avoided. Thus, large time delays are feasible though at increasing losses.

Further investigations are needed to determine the experimental limits of group velocity reduction. The backscattering in this case is a most important effect that should be taken into account.

8. Conclusion and outlook

8.1 Conclusion

This thesis combines a complete theoretical investigation of the slow light phenomenon in line defect photonic crystal waveguides starting from dispersion characteristics of the ideal structures and finishing with coupling design and backscattering loss discussion. A commercial finite integration software was extensively used to check the theoretical models. Several useful supplementary models based on transfer matrix method and eigenmodes expansion are developed to describe the Bloch mode propagation and reflection in photonic crystal structures.

First, the effect of small group velocity in photonic crystal line-defect waveguides was investigated. As was originally shown the interaction with the triangular lattice photonic crystal structure of the waveguide walls leads to a strong group velocity reduction. An approach is presented for the first time to obtain small group velocity line defects waveguide with vanishing second and third order dispersion on a finite bandwidth. For example, for the group velocity 0.02c the bandwidth of 1THz can be obtained. The group velocity can be further decreased with approximately proportionally decreasing bandwidth. Remarkable is the fact that these properties are obtained by simple variation of the waveguide width and radius of the holes. It should be mentioned that quasi constant group velocities are not tunable and can be adjusted only for certain normalized frequencies. Any parameter variation changes not only the group velocity but also the normalized frequency of the mode. The operational frequency can be adjusted by the lattice parameter of the structure, but it cannot be tuned afterwards. But for the time delay or phase shift tuning purposes simply the length of the slow light region can be arbitrary decreased by shifting the slow light bandwidth from the operational frequency.

Large positive and negative dispersion can be obtained due to the modes anti-crossings in single and coupled line-defect waveguides or by introduction of linear chirp on single or coupled line-defect waveguides. It was demonstrated in this thesis that in line-defect waveguides there are sufficient structural parameters to design various dispersion characteristics.

In this thesis a very efficient coupling approach to slow light modes is presented. The coupling from dielectric strip waveguide through a section of a line-defect waveguide with index guided mode is used. This allows a dramatic reduction of the scattering loss with reflection about -20dB and transmission of almost 95% for 0.02c group velocity. These results can be achieved with a line-defect waveguide about five lattice constants long which has a somewhat larger waveguide width and the same radius of the holes. Any further improvement is probably not necessary for most of the applications. But when a smaller reflection intensity is required, adiabatic coupling can be applied. With a proper taper function the dramatic reflection reduction can be achieved already within 20 lattice constants.

Slow light in a waveguide without dispersion and coupling losses would be a perfect candidate for many applications if it were possible to manufacture structures without inaccuracies. Disorder can be a most important problem for implementation of slow light waveguides. Disorder induced losses originate from vertical and backscattering of the waveguide modes. The vertical scattering was not investigated in this thesis but it is expected that backscattering is a dominating loss mechanism at small group velocities. Accordingly strong backscattering was estimated at small group velocities. The localization phenomena were also discussed which are even more problematic than just intensity losses. Further experimental and simulation investigations are required to address the effects of backscattering and localization. Though from results obtained in this thesis and other publications it is difficult to expect slow light structures longer than 100μm.

The dispersion of -2000ps/nm with bandwidth of 100GHz can be obtained in a structure smaller than 1cm. This dispersion is sufficient for 100km fiber dispersion compensation. However, these considerations are valid only for ideal waveguides without disorder. In the dispersion compensation structure different frequencies propagate with different group velocities. Thus there is strong frequency dependent loss that can lead to additional signal distortion. Time delay of 0.3ns on 100GHz bandwidth is theoretically possible in an ideal photonic crystal structure of 1 mm. This can be achieved in a single slow light waveguide or chirped coupled waveguide structure. But once again the disorder limits the lengths of the structures dramatically. Thus the application of slow light waveguides to dispersion compensation and time delay depends on the future disorder reduction. Fortunately, the scattering intensity scales with disorder parameter squared. Thus double precision leads to four times loss reduction.

8.2   Outlook

The slow light investigations presented in this thesis can be extended in different directions. Some of the possible experiments and concepts are proposed further in this section. Though it should be mentioned again that most of the application of slow light strongly depend on the disorder induced losses.

Slow light demonstration: The measurement of slow light in line-defect waveguides with optimized double stage couplers is a very promising experiment. It will be a first demonstration of small group velocity in a line-defect waveguide with vanishing dispersion and very small coupling loss. The group velocity can be measured from the periods of MZI interference similar to the method applied in the paper of Vlasov et al. [7].

Scattering loss measurements: This measurement is very important for the following application of slow light waveguides. The scattering loss can be estimated from a cut back method [25]. If the double stage coupler is used the coupling loss can be neglected.

Tunable time delay: The time delay can be tuned with a variation of the group velocity or propagation length. A simple approach would be a single waveguide with length variation. The slow light waveguide with vanishing dispersion can be used where the length of the slow light section can be changed with, for example, temperature or deformation. In the section with changed parameters the mode is shifted from slow light bandwidth into "index guided" bandwidth. Thus time delay will be mostly defined by the slow light section, the length of which can be changed. The transition parts from index guide into slow light section and back will be automatically adiabatic due to the distributed nature of temperature or deformation tuning. Another possibility for length variation is the coupled waveguides scheme. Slow light and normal line-defect waveguides can run parallel to each other. The coupling between them is achieved only at two points where parameters are shifted. By changing the distant between the coupling points the length variation is achieved.

Tunable dispersion compensation: Chirped periodical structures are most promising for dispersion compensation. The difficulty of a single waveguide structure is that input coincides with input waveguide. It is favorable to design coupled waveguides structure where input and output are separated. That would eliminate time delay ripples appearing due to the Gires-Tournois interference and would allow operation without optical circulators.

Miniaturization of Mach Zehnder interferometer : Small parameter variations of slow light waveguide lead to the change of accumulated phase proportional to group velocity. Thus the length of a MZI switch can be reduced proportional to the group velocity reduction. The concept similar to presented in [17] can be used, but with quasi constant group velocity and optimized coupling.

Integration with slot waveguide: The recently presented concept of electrooptical tuning with slot waveguides [87][88] can be enhanced with slow light waveguides. First, the line-defect waveguide provides electrical coupling to the waveguide center

through photonic crystal claddings. At the same time light deceleration leads to amplitude increase, which is favorable for the electrooptical interaction.

References

[1] G. P. Agrawal, Fiber-Optic Communication Systems, 2nd ed., New York, Wiley, 1997

[2] P. Herve, S. Ovadia, "Optical Technologies for Enterprise Networks," *Intel Technol. J.*, vol. 8, pp. 73-82, May 2004

[3] D. Miller, "Rationale and challenges for optical interconnects to electronic chips", *Proc. IEEE*, vol. 88, pp. 728-749, June 2000

[4] K.-P. Ho, Phase-Modulated Optical Communication Systems, Springer, New York, 2005

[5] R. Ramaswami and K. Sivarajan, Optical Networks: A Practical Perspective, 2nd ed., San Mateo, CA, Morgan Kaufmann, 2001

[6] M. Notomi, K. Yamada, A. Shinya, J. Takahashi, C. Takahashi, and I. Yokohama, "Extremely large group-velocity dispersion of line-defect waveguides in photonic crystal slabs," *Phys. Rev. Lett.*, vol. 87, pp. 253902 1-4, Dec 2001

[7] Y. A. Vlasov, M. O'Boyle, H. F. Hamann, and S. J. McNab, "Active control of slow light on a chip with photonic crystal waveguides," *Nature*, vol. 438, pp. 65-69, Nov 2005

[8] D. Mori and T. Baba, "Wideband and low dispersion slow light by chirped photonic crystal coupled waveguide," *Opt. Express*, vol. 13, pp. 9398-9408, Nov 2005

[9] R. J. P. Engelen, Y. Sugimoto, Y. Watanabe, J. P. Korterik, N. Ikeda, N. F. van Hulst, K. Asakawa, and L. Kuipers, "The effect of higher-order dispersion on slow light propagation in photonic crystal waveguides," *Opt. Express*, vol. 14, pp. 1658-1672, Feb 2006

[10] M. Povinelli, S. Johnson, and J. Joannopoulos, "Slow-light, band-edge waveguides for tunable time delays," *Opt. Express*, vol. 13, pp. 7145-7159 Sept 2005

[11] H. Gersen, T. J. Karle, R. J. P. Engelen, W. Bogaerts, J. P. Korterik, N. F. van Hulst, T. F. Krauss, and L. Kuipers, "Real-space observation of ultraslow light in photonic crystal waveguides," *Phys. Rev. Lett.*, vol. 94, pp. 073903, Feb 2005

[12] L. V. Hau, S. E. Harris, Z. Dutton, and C. H. Behroozi, "Light speed reduction to 17 metres per second in an ultracold atomic gas," *Nature*, vol. 397, pp. 594-598, Feb 1999

REFERENCES

[13] M. D. Lukin and A. Imamoglu, "Controlling photons using electromagnetically induced transparency," *Nature*, vol. 413, pp. 273-276 Sept 2001

[14] R. S. Tucker, P. -C. Ku, and C. J. Chang-Hasnain, "Slow-Light Optical Buffers: Capabilities and Fundamental Limitations," *J. Lightwave Technol.*, vol. 23, pp. 4046-4066, Dec 2005

[15] B. Khurgin, "Optical buffers based on slow light in electromagnetically induced transparent media and coupled resonator structures: comparative analysis," *J. Opt. Soc. Am. B*, vol. 22, pp. 1062-1074, May 2005

[16] Y. Sugimoto, Y. Tanaka, N. Ikeda, Y. Nakamura, K. Asakawa, and K. Inoue, "Low propagation loss of 0.76 dB/mm in GaAs-based single-line-defect two-dimensional photonic crystal slab waveguides up to 1 cm in length," *Opt. Express*, vol. 12, pp. 1090-1096, March 2004

[17] Y. Jiang, W. Jiang, L. Gu, X. Chen, R. T. Chen, "80-micron interaction length silicon photonic crystal waveguide modulator", *Appl. Phys. Lett.*, vol: 87, pp. 221105, Nov 2005

[18] A. Yariv, Y. Xu, RK Lee, and A. Scherer, "Coupled-resonator optical waveguide: a proposal and analysis," *Opt. Lett.,* vol. 24, pp. 711–713,. June 1999

[19] P. Russell, "Optics of Floquet-Bloch waves in dielectric gratings," *Appl. Phys. B*, vol. 39, pp 231-246, 1986

[20] S. John, "Strong localization of photons in certain disordered dielectric superlattices," *Phys. Rev. Lett.*, vol. 58, pp. 2486-2489, June 1987

[21] E. Yablonovitch, "Inhibited spontaneous emission in solid-state physics and electronics," *Phys. Rev. Lett.*, vol. 58, pp. 2059-2062, May 1987

[22] R. Zengerle, "Light propagation in singly and doubly periodic planar waveguides," *J. Mod. Optics.*, vol. 34, pp. 1589–1617, 1987

[23] S. G. Johnson, P. R. Villeneuve, S. Fan, and J. D. Joannopoulos, "Linear waveguides in photonic-crystal slabs," *Phys. Rev. B*, vol 62, pp. 8212-8222, Sept 2000

[24] M. Loncar, J. Vuckovic, and A. Scherer, "Methods for controlling positions of guided modes of photonic-crystal waveguides," *J. Opt. Soc. Am. B*, vol. 18, pp. 1362-1368, Sept 2001

[25] S. J. McNab, N. Moll, and Yu. A. Vlasov, "Ultra-low loss photonic integrated circuit with membrane-type photonic crystal waveguides", *Opt. Express,* vol. 11, pp. 2927-2939, Nov 2003

[26] M. Notomi, A. Shinya, S. Mitsugi, E. Kuramochi, and H-Y. Ryu, "Waveguides, resonators and their coupled elements in photonic crystal slabs," *Opt. Express*, vol. 12, pp. 1551-1561, Apr 2004

[28] D. Mori and T. Baba, "Dispersion-controlled optical group delay device by chirped photonic crystal waveguides," *Appl. Phys. Lett.*, vol. 85, pp. 1101-1103, Aug 2004

[27] M. Soljacic, S. G. Johnson, S. Fan, M. Ibanescu, E. Ippen, and J. D. Joannopoulos, "Photonic-crystal slow-light enhancement of nonlinear phase sensitivity ," *J. Opt. Soc. Am. B*, vol. 19, pp. 2052-2059, Sept 2002

[29] K. Hosomi and T. Katsuyama, "A dispersion compensator using coupled defects in a photonic crystal," *IEEE J. Quantum Electron.*, vol. 38, pp. 825-829, July 2002

[30] S. G. Johnson, S. Fun, P. Villeneuve, J. Joannopoulos, and L. Kolodziejski, "Guided modes in photonic crystal slabs," *Phys. Rev. B*, vol. 60, pp. 5751-5758, Aug 1999

[31] G. T. Reed and A. P. Knights, "Silicon Photonics: An Introduction", Wiley, Chichester, UK, 2004

[32] L. Pavesi and D. J. Lockwood, "Silicon Photonics", Springer-Verlag, New York, 2004

[33] Q. Xu, B. Schmidt, S. Pradhan, and M. Lipson, "Micrometre-scale silicon electro-optic modulator," *Nature*, vol. 435, pp. 325-327, May 2005

[34] H. Rong, R. Jones, A. Liu, O. Cohen, D. Hak, A. Fang, and M. Paniccia, "A Continuous-Wave Raman Silicon Laser," *Nature*, vol. 433, pp. 725-728, Feb 2005

[35] K. Sasaki, F. Ohno, A. Motegi, and T. Baba, "Arrayed waveguide grating of 70x60 μm^2 size based on Si photonic wire waveguides", *Electron. Lett.*, vol. 41, pp. 801-802, July 2005

[36] J. Joannopoulos, R. Meade, and J. Winn, *Photonic Crystals*, Princeton: Princeton Univ., 1995

[37] S. Noda, K. Tomoda, N. Yamamoto, and A. Chutinan, "Full three-dimensional photonic bandgap crystals at near-infrared wavelengths," *Science*, vol. 289, pp. 604-606, July 2000

[38] M. Qi, E. Lidorikis, P. T. Rakich, S. G. Johnson, J. D. Joannopoulos, E. P. Ippen, and H. I. Smith, "A threedimensional optical photonic crystal with designed point defects," *Nature*, vol. 429, pp. 538-542, June 2004

REFERENCES

[39] J. M. Bendickson, J. P. Dowling, M. Scalora, "Analytic expressions for the electromagnetic mode density in finite, one-dimensional, photonic band-gap structures," *Phys. Rev. E*, vol. 53, pp. 4101-4121, April 1996

[40] A. Yariv and P. Yeh, Optical waves in crystals, New York: Wiley, 1984

[41] P. Bienstman, Rigorous and Efficient Modelling of Wavelength Scale Photonic Components, doctoral dissertation 2001, Ghent University, Belgium. Available online at http://photonics.intec.rug.ac.be/download/phd_104.pdf

[42] P. Bienstman and R. Baets, "Optical modelling of photonic crystals and VCSELs using eigenmode expansion and perfectly matched layers," *Opt. Quantum. Electron.*, vol 33, pp. 327–341, 2001

[43] http://camfr.sourceforge.net/

[44] G. Boettger, Finite integration simulations of photonic crystal structures for microphotonics devices, doctoral dissertation 2005, Hamburg University of Technology, Germany

[45] M. Clemens and T. Weiland, "Discrete electromagnetism with the finite integration technique", *Progress in Electromagn. Research PIER*, vol. 32, pp. 65-87, 2001

[46] S. Mookherjea and A. Yariv, "Pulse propagation in a coupled resonator optical waveguide to all orders of dispersion," *Phys. Rev. E*, vol. 65, pp. 0566011 1-6, April 2002

[47] A. Adibi, Y. Xu, R. K. Lee, M. Loncar, A. Yariv, and A. Scherer, "Role of distributed Bragg reflection in photonic-crystal optical waveguides," *Phys. Rev. B 64*, pp. 041102(1-4), July 2001

[48] U. Peschel, T. Peschel, and F. Lederer, "A compact device for highly efficient dispersion compensation in fiber transmission," *Appl. Phys. Lett.*, vol. 67, pp. 2111-2113, Oct 1995

[49] T. D. Engeness, M. Ibanescu, S. G. Johnson, O. Weisberg, M. Skorobogatiy, S. Jacobs, and Y. Fink, "Dispersion tailoring and compensation by modal interactions in OmniGuide fibers," *Opt. Express*, vol. 11, pp. 1175-1196, May 2003

[50] T. Sondergaard and K. Dridi, "Energy flow in photonic crystal waveguides," *Phys. Rev. B*, vol. 61, pp. 15 688-696, June 2000

[51] S. G. Johnson, P. Bienstman, M. A. Skorobogatiy, M. Ibanescu, E. Lidorikis, and J. D. Joannopoulos, "Adiabatic theorem and continuous coupled-mode theory for efficient taper transitions in photonic crystals," *Phys. Rev. E*, vol. 66, pp. 066608 1-15, Dec 2002

[52] F. Ouellette, "Dispersion cancellation using linearly chirped Bragg grating filters in optical waveguides," *Opt. Lett.*, vol. 12, pp. 847-849, Oct 1987

[53] C. K. Madsen and G. Lenz, "Optical all-pass filters for phase response design with applications for dispersion compensation," *IEEE Photon. Technol. Lett.*, vol. 10, pp. 567-569, July 1999

[54] C. K. Madsen, G. Lenz, A. J. Bruce, M. A. Cappuzzo, L. T. Gomez, and R. E. Scotti, "Integrated all-pass filters for tunable dispersion and dispersion slope compensation," *IEEE Photon. Technol. Lett.*, vol. 11, 1623-1625, Dec 1999

[55] N. M. Litchinitser, B. J. Eggleton, and D. B. Patterson, "Fiber Bragg gratings for dispersion compensation in transmission: theoretical model and design criteria for nearly ideal pulse recompression," *J. Light. Tech.*, vol. 15, pp. 1303-1313, Aug 1997

[56] T. Baba, D. Mori, K. Inoshita, and Y. Kuroki, "Light localizations in photonic crystal line defect waveguides," *IEEE J. Sel. Quantum Electron.*, vol. 10, pp. 484-491, May 2004

[57] T. A. Ramadan, R. Scarmozzino, and R. M. Osgood, "Adiabatic couplers: design rules and optimization," *J. Light. Tech.*, vol. 16, pp. 277-283, Feb 1998

[58] R. Szipöcs, K. Ferenc, Ch. Spielmann, and F. Krausz, "Chirped multilayer coatings for broadband dispersion control in femtosecond lasers," *Opt. Lett.*, vol. 19, pp. 201-203, Feb 1994

[59] N. Matuschek, F. Kärtner, and U. Keller, "Theory of double-chirped mirrors," *IEEE J. Sel. Quantum Electron.*, vol. 4, pp. 197-208, March 1998

[60] G. Lenz, B. Eggleton, C.R. Giles, C.K. Madsen, and R.E. Slusher, "Dispersive Properties of Optical Filters for WDM Systems," *J. Quantum Electron.*, vol. 34, pp. 1390-1402, Aug 1998

[61] J. Zimmermann, M. Kamp, A. Forchel, and R. März, "Photonic crystal waveguide directional couplers as wavelength selective optical filters," *Optics Communications*, vol. 230, pp. 387-392, 2004

[62] T. Koponen, A. Huttunen, and P. Törmä, "Conditions for waveguide decoupling in square-lattice photonic crystals," *J. Appl. Phys.*, vol. 96:4041, 2004

[63] C. Martijn de Sterke, L. C. Botten, A. A. Asatryan, T. P. White, and R. C. McPhedran, "Modes of coupled photonic crystal waveguides," *Opt. Lett.*, vol. 29, 1384-1386, June 2004

[64] S. Boscolo, M. Midrio, and C. G. Someda, "Coupling and decoupling of electromagnetic waves in parallel 2-D photonic crystal waveguides," *IEEE J. Quantum Electron.*, vol. 38, 47-53, Jan 2002

[66] N. Matuschek, F. Kärtner, and U. Keller, "Exact coupled-mode theories for multilayer interference coatings with arbitrary strong index modulations", *IEEE J. Quantum Electron.*, vol. 33, pp. 295-302, March 1997

[65] D. Marcuse, *Theory of Dielectric Optical Waveguides*, 2nd ed. New York: Academic, 1991

[67] M. Parker and D. Walker, "Arrayed waveguide gratings, fiber Bragg gratings, and photonic crystals: an isomorphic Fourier transform light propagation analysis," *IEEE J. Sel. Quantum Electron.*, vol. 8, pp. 1158-1167, Nov 2002

[68] M. Parker and D. Walker, "A unified Fourier transform theory for photonic crystal and FBG filters in the strong coupling regime," *IEEE Photon. Technol. Lett.*, vol. 14, pp. 1321-1323, Sept 2002

[69] P. Russell and T. Birks, "Hamiltonian optics of nonuniform photonic crystals," *J. Light. Tech.*, vol. 17, pp. 1982-1988, Nov 1999

[70] B. J. Eggleton, P. A. Krug, L. Poladian, K. A. Ahmed, and H.-F. Liu, "Experimental demonstration of compression of dispersed optical pulses by reflection from self-chirped optical fiber Bragg gratings," *Opt. Lett.,* vol. 19, pp. 877–879, June 1994

[71] G. Steinmeyer, "Dispersion oscillations in ultrafast phase-correction devices," *IEEE J. Quantum Electron.*, vol. 39, pp. 1027-1034, Aug 2003

[72] Y. A. Vlasov and S. J. McNab, "Coupling into the slow light mode in slab-type photonic crystal waveguides," *Opt. Lett.*, vol. 31, pp. 50-52, Jan 2006

[73] M. Palamaru and Ph. Lalanne, "Photonic crystal waveguides: out-of-plane losses and adiabatic modal conversion," *Appl. Phys. Lett.*, vol. 78, pp. 1466-69, March 2001

[74] A. Mekis and J. D. Joannopoulos, "Tapered Couplers for Efficient Interfacing Between Dielectric and Photonic Crystal Waveguides," *J. Lightwave Technol.*, vol 19, pp. 861-865, June 2001

[75] P. Bienstman, S. Assefa, S. G. Johnson, J. D. Joannopoulos, G. S. Petrich, and L. A. Kolodziejski, "Taper structures for coupling into photonic crystal slab waveguides ," *J. Opt. Soc. Am. B*, vol. 20, pp. 1817-1821 Sept 2003

[76] P. Sanchis, P. Bienstman, B. Luyssaert, R. Baets, and J. Marti, "Analysis of buttcoupling in photonic crystals," *IEEE J. Quantum Electron.*, vol. 40, pp. 541-550, May 2004

[77] J. Ushida, M. Tokushima, M. Shirane, A. Gomyo, and H. Yamada, "Immittance matching for multidimensional open-system photonic crystals," *Phys. Rev. B*, vol. 68, pp. 155115-155121, Oct 2003

[78] Y. Tanaka, Y. Sugimoto, N. Ikeda, H. Nakamura, K. Asakawa, K, Inoue, and S. G. Johnson, "Group velocity dependence of propagation losses in single-line-defect photonic crystal waveguides on GaAs membranes," *Electron. Lett.*, vol. 40, pp. 174-176, Feb 2004

[79] D. Gerace and L. C. Andreani, "Disorder-induced losses in photonic crystal waveguides with line defects," *Opt. Lett.*, vol. 29, pp. 1897–1899, Aug 2004

[80] S. Hughes, L. Ramunno, J. F. Young, and J. E. Sipe, "Extrinsic optical scattering loss in photonic crystal waveguides: role of fabrication disorder and photon group velocity," *Phys. Rev. Lett.*, vol. 94, pp. 033903, Jan 2005

[81] E. Kuramochi, M. Notomi, S. Hughes, A. Shinya, T. Watanabe and L. Ramunno, "Disorder-induced scattering loss of line-defect waveguides in photonic crystal slabs," *Phys Rev B.*, vol. 72, pp. 161318, Oct 2005

[82] L. C. Andreani, D. Gerace, and M. Agio, "Gap maps, diffraction losses and exciton-polaritons in photonic crystal slabs," *Phot. Nanostruct.*, vol. 2, pp. 103–110, Aug 2004

[83] S.G. Johnson, M.L. Povinelli, P. Bienstman, M. Skorobogatiy, M. Soljacic, M. Ibanescu, E. Lidorikis, J.D. Joannopoulos, "Coupling, scattering, and perturbation theory: semi-analytical analyses of photonic-crystal waveguides" in *Proc. 2003 5th Intl. Conf. on Transparent Optical Networks and 2nd European Symp. on Photonic Crystals*, vol. 1, pp. 103-109, 2003

[84] D Wiersma, P. Bartolini, A. Lagendijk, and R. Righini, "Localization of light in a disordered medium", *Nature*, vol. 390, pp. 671-673, Dec 1997

[85] S. G. Johnson, M. L. Povinelli, M. Soljacic, A. Karalis, S. Jacobs, and J. D. Joannopoulos, "Roughness losses and volume-current methods in photonic-crystal waveguides," *J. Appl. Phys. B*, vol. 81, pp. 283–293, July 2005

[86] D. Gerace and L. Andreani, "Low-loss guided modes in photonic crystal waveguides," *Opt. Express*, vol. 13, pp. 4939-4951, June 2005

[87] V. R. Almeida, Qianfan Xu, C. A. Barrios and M. Lipson, "Guiding and confining light in void nanostructure," *Opt. Lett.*, vol. 29, pp. 1209-11 , June 2004

[88] T. Baehr-Jones, M. Hochberg, G. Wang, R. Lawson, Y. Liao, P. Sullivan, L. Dalton, A. Jen, and A. Scherer, "Optical modulation and detection in slotted Silicon waveguides," *Opt. Express*, vol. 13, pp. 5216-5226, July 2005

List of Publications

Papers:

- M. Schmidt, A. Petrov, J. Wülbern, M. Eich, U. Huebner and R. Boucher, "Modulation and dispersion control in photonic crystals", *Proc. SPIE Linear and Nonlinear Optics of Organic Materials VI*, **6331**, 633109 (2006)

- J. H. Wülbern, M. Schmidt, M. Eich and U. Hübner, "Electrooptically Tunable Photonic Crystals", *Proc. SPIE Photonic Crystal Materials and Devices III*, **6182**, 618210 (2006)

- A. Petrov and M. Eich, "Efficient Approximation to Calculate Time Delay and Dispersion in Linearly Chirped Periodical Microphotonic Structures", *J. Quantum Electron.*, **41**, 1502 (2005)

- A. Petrov and M. Eich, "Large second order dispersion in periodical and aperiodical photonic crystal waveguides", *Proc. SPIE Nanophotonics for Communication: Materials and Devices II*, **6017**, 601708 (2005)

- A. Petrov and M. Eich, "Dispersion compensation with photonic crystal line-defect waveguides", *IEEE J. Select. Areas Commun.* Nanotechnologies for communications, **23**, 1396 (2005)

- A. Petrov and M. Eich, "Zero dispersion at small group velocities in photonic crystal waveguides", *Appl. Phys. Lett.*, **85**, 4866-4868 (2004)

- M. Schmidt, G. Böttger, C. Liguda, A. Petrov, K. Mellert, M. Eich et al., "Tuneable Polymer Photonic Crystals", *Linear and Nonlinear Optics of Organic Materials III SPIE*, **5212**, 171 (2003)

Book article:

- M. Augustin, G. Böttger, M. Eich, A. Petrov et al., "Photonic crystal optical circuits in moderate index materials", Photonic Crystal – Advances in Design, Fabrication and Characterization, Ed.: K. Busch, R. Wehrspohn, H. Föll, Wiley-VCH, Berlin (2003)

Presentations and posters:

- J. Brosi, W. Freude, J. Leuthold, A. Yu. Petrov, M. Eich, "Broadband Slow Light in a Photonic Crystal Line Defect Waveguide", OSA Topical Meeting on Slow and Fast Light (SL'06), Washington (DC), USA, July 23–26, 2006 (talk)

- M. Schmidt, A. Petrov, J. Wülbern, and M. Eich, "Modulation and Dispersion Control in Photonic Crystals", SPIE Optics and Photonics 2006, San Diego, USA, August 13-17, 2006 (talk)

- A. Petrov, J. Wülbern, and M. Eich, "Investigations of microphotonic structures with CST Microwave Studio", CST User Group Meeting, Darmstadt, Germany, March 8-9, 2006 (talk)

- A. Petrov and M. Eich, "Large second order dispersion in periodical and aperiodical photonic crystal waveguides", Optics East 2005, Boston, Massachusetts, USA, October 23-26, 2005 (invited talk)

- A. Petrov, M. Schmidt and M. Eich, "Electrooptically Tunable Photonic Crystals and Dispersion Properties of Line-defect Waveguides", COST P11 meeting, Twente, Netherlands, Oktober 2-4, 2005 (invited talk)

- A. Petrov and M. Eich, "Small group velocity photonic crystal waveguides for group delay and dispersion management", PECS-VI, Aghia Pelaghia, Crete, Greece, June 19-24, 2005 (poster)

- A. Petrov and M. Eich, "Dispersion properties of coupled mode in photonic crystal waveguides", DPG 69th annual meeting, Berlin, Germany, March 4-9, 2005 (talk)

- A. Petrov and M. Eich, "Dispersion and group velocity control in photonic crystal linear waveguides", Basic Problems of Optics Conference, Saint-Petersburg, Russia, October 18-21, 2004 (talk)

- A. Petrov, M. Schmidt, G. Böttger and M. Eich, "Photonic crystals simulations with CST Microwave Studio", CST European User Group Meeting, Darmstadt, Germany, September 23-24, 2004 (poster)

- A. Petrov and M. Eich, "Dispersion control with photonic crystal waveguides ", 10th Microoptic Conference, Jena, Germany, September 1-3, 2004 (talk)

- A. Petrov, K. Preusser-Mellert, M. Schmidt, G. Böttger and M. Eich, "Photonic crystals for compact dispersion compensators", PECS-V, Kyoto, Japan, March 2004 (poster)

Acknowledgements

Curriculum vitae

Name: Alexander Petrov
Date of Birth: August, 8th 1978
Birthplace: Saint Petersburg, Russia

Education

Sept 1985 - June 1995   Secondary schools 71, 76 and 98, St. Petersburg

Sept 1995 - June 2000   St. Petersburg State Polytechnical University (SPbSPU),
                           Bachelor of Science in Technical Physics, 1999

Aug 2000 - Jan 2003   Northern Institute of Technology (NIT), Hamburg
                           Program in Management, Law and Humanities
                           Professional Master in Global Technology Management,
                           2003

Oct 2000 - March 2003   Hamburg University of Technology (TUHH)
                           Master of Science in Material Science, 2003

May 2003 - July 2006   Hamburg University of Technology (TUHH)
                           Slow light photonic crystal line-defect waveguides
                           Prof. Dr. M. Eich
                           PhD in Microphotonics

Work experience

Oct 2006 - Dec 2007   McKinsey & Company, Moscow
                           Junior Associate

since Feb 2008   Hamburg University of Technology (TUHH)
                           Associate professor (Oberingenieur)